Constrictional flow and strain partitioning during oblique deformation: insights from the Variscan Tanneron massif, SE France

J. Gremmel[1*], G. Duclaux[1], M. Corsini[1], J. Bascou[2]

[1]Université Côte d'Azur, CNRS, Observatoire de la Côte d'Azur, IRD, Géoazur, 250 rue Albert Einstein, Sophia Antipolis 06560 Valbonne, France

[2]Université Jean Monnet, CNRS, LGL-TPE UMR5276, F-42023, Saint-Etienne, France

**Corresponding author (e-mail : gremmel@geoazur.unice.fr)*

The present manuscript is a non-peer reviewed preprint submitted to EarthArXiv. The preprint was submitted to Tektonika journal for peer review.

Abstract

Structural analysis through precise digital mapping combined with microstructural and quantitative finite strain data were used to investigate strain partitioning and strain shape evolution during the late-stage oblique tectonic collapse of a hot orogen. The Tanneron massif in SE France was structured in an oblique tectonic regime at the end of the Variscan orogeny, leading to the exhumation of lower to middle crustal migmatite terrains. Strain patterns show prominent stretching lineations associated with L>S tectonites and dextral strike-slip SZ compatible with subsimple shear deformation. The overall kinematic with pure shear sub-horizontal constrictional flow and sub-vertical simple shear-dominated transcurrent corridors depict a transtensional regime. The progressive transtensional deformation event evolves through two successive intermediate phases, the first characterised by a dominant sub-horizontal flow of the ductile crust represented by gently dipping foliation and L>S tectonites associated to widespread sub-horizontal stretching lineations followed by a second plane strain flow associated with vertical foliation and S-L tectonites. Finite strain analysis confirms the monotony of the L>S and S-L tectonites and highlights a partly lithological control on the finite strain ellipsoid shape with meta-igneous units defining L>S fabrics while meta-sedimentary units depict S-L fabrics. Microstructural observations also constrain the temperature evolution of the

progressive transtensional deformation. Sub-horizontal flow starts at supra-solidus conditions and progresses to sub-vertical shear down to greenschist facies solely in hydrated meta-sedimentary units. We propose a rheologically driven strain path partitioning during the progressive exhumation of this deep crust throughout a two-phase transtensional regime.

1. Introduction

Oblique tectonic systems, characterised by the combination of strike-slip and compressional or extensional components, are widespread on Earth and have become more commonly described as our understanding of geologic structures advances (Dewey 2002; Dewey et al., 1998; Fossen and Tikoff, 1993, 1998; Harland, 1971; Oldow et al., 1990; Sanderson and Marchini, 1984; Teyssier and Tikoff, 1999). These systems, including transpression and transtension end-members, have been extensively studied in the brittle crust, with a focus on seismic implications and specific structures such as pull-apart basins, en-echelon folds, and faults arrays (Alvarado et al., 2011; Asti et al., 2022; Autin et al., 2010; Brune, 2014; Chorowicz and Sorlien, 1992; De Paola et al., 2005; Duclaux et al., 2020; Ferranti, 2009; Meghraoui and Pondrelli, 2012; Morley et al., 2004; Norris et al., 1990; Richard et al., 1995; Schreurs and Colletta, 1998; Umhoefer and Dorsey, 1997; Wilson et al., 2006; Withjack and Jamison, 1986). On the scale of tectonic plates, the San Andreas fault in California (Sylvester and Smith, 1976; Teyssier and Tikoff, 1998), the Alpine fault in New-Zealand (Cashman et al., 1992; Teyssier et al., 1995) and the Great Sumatran faults in Sumatra (Mount and Suppe, 1992; Tikoff and Teyssier, 1994) represent worldwide studied examples of oblique plate motion. However, research on oblique tectonics in the ductile domain of the middle to lower crust reveals a structural complexity that make fabrics interpretation challenging (Archanjo et al., 2002; Bascou et al., 2023; Chardon et al., 2009, 2011; Clegg and Holdsworth, 2005; Faleiros et al., 2022; Gapais et al., 2008; Gébelin et al., 2007; Klepeis et al., 2022; Paulsen et al., 2004; Wiest et al., 2019), especially in the context of hot orogens. Studies are mainly confined to Precambrian orogens and remain scarce in Phanerozoic systems. Furthermore, these studies mostly focus on strain analysis within the transpressional regime, whereas transtension remains poorly understood, yet it should play a key role during orogenic collapse in order to progressively thin orogens.

In this study, we aim to provide a detailed description of strain shape and partitioning evolutions within an oblique tectonic regime in the context of late-stage evolution of a Phanerozoic hot orogen. We investigate the development of crustal fabrics formed by oblique tectonic flow in the Variscan belt, exposed by the most internal part of the Maures-Tanneron massif in SE France. By combining structural analysis through detailed field mapping, microstructural observations, and finite strain and tectonite calculations, we define the three-dimensional kinematic framework of a transtensional flow in the Carboniferous basement of the Tanneron massif.

Our results show that widespread gently dipping constrictional fabrics associated with vertical strike-slip shear zones are produced in transtension. In detail, two distinct strain patterns defined by different tectonic fabrics and contrasting deformation temperatures are evidenced, and show lithological-dependent distribution. We propose that strain partitioning and localisation are partly controlled by rheological contrasts between ortho- and paragneisses during exhumation and retrograde deformation. Orthogneiss units preferentially preserve the initial high-temperature constrictional stage, while the subsequent lower-temperature strike-slip stage is preferentially localised in the weaker paragneiss units. This study contributes to a better understanding of the complex processes and structures involved in oblique tectonic regimes within ductile crustal environments. The described tectonic evolution represents a good example of a kinematic framework during the exhumation of the internal part of a collapsing orogen.

2. Geological setting

2.1 Maures-Estérel-Corsica-Sardinia micro-plate (MECS)

The Maures-Tanneron-Massif (MTM) represents the southernmost segment of the Variscan belt in France's mainland and belongs to the MECS ("Maures-

Estérel-Corsica-Sardinia") micro-plate (Edel et al., 2018). The Corsica-Sardinia block rifted apart the MTM during the Miocene Mediterranean back-arc extensional event by a 45° to 55° anticlockwise rotation (Gattacceca, 2000). Along the Mediterranean Sea, the MTM extends from Toulon in the Southwest to Cannes in the Northeast forming a 90 km long and 50 km wide belt (Fig. 1).

The MTM is defined as a subduction-collision belt active from 420 to 300 Ma (Schneider et al., 2014). After the subduction event, the collisional stage between 360-330 Ma (Oliot et al., 2015; Schneider et al., 2014) is responsible of the MTM structuration in N-S litho-tectonic units following an increasing metamorphic gradient from West to East (Rolland et al., 2009). Metamorphic isograds progress from chlorite zone, to garnet-chlorite, biotite-staurolite, biotite-kyanite, and finally biotite-muscovite-sillimanite zone (Buscail, 2000). Therefore, the belt is divided in two domains: the external domain to the West with low grade metamorphic rocks, and the internal domain to the East only composed of migmatitic units (Fig. 1). At the end of this collisional stage, a first partial melting event and associated calc-alkaline magmatism is documented between 340-330 Ma (Oliot et al., 2015). In the internal domain, a gneiss dome structure juxtaposed to the Rouet granite intrusion associated with pervasive vertical strike-slip shear zones dated between 325 and 300 Ma have been interpreted as the result of a regional transpressive event marking the waning of the orogenic cycle (Corsini et al., 2009; Rolland et al., 2009). This latter deformation event has largely overprinted preexisting fabrics. In

Sardinia, this oblique deformation event has also been dated between 320 and 300 Ma (Carosi et al., 2012). At the scale of the MECS, this oblique deformation is mostly interpreted as a transpressional regime (MTM: Rolland et al., 2009, Simonetti et al., 2020; Sardinia: Carosi et al., 2020; Frassi et al., 2009), while some authors described a transtensional regime (MTM: Buscail, 2000; Corsica: Thevoux-Chabuel et al., 1995). Widespread granitoid and related dykes emplaced synchronously with this late event in the Maures-Tanneron massif (Bolle et al., 2023; Corsini et al., 2010; Duchesne et al., 2013).

Finally, thinning and exhumation of the migmatitic units are accompanied by late Carboniferous pull-apart basins opening along major North-South crustal shear zones (SZ) (Fig. 1): the Plan-de-la-tour basin along the Grimaud SZ (Onezime et al., 1999) and the Reyran basin along the La Moure SZ (Toutin-Morin et al., 1994). These narrow N-S intramontane hemi-graben basins consist of folded coarse detrital sediments filled by the erosion product of the surrounding migmatitic units alternating with lignite layers (Maillet, 2021). These basins are thought to open between 315 and 298 Ma (Toutin-Morin et al., 1994) synchronously and parallel to the basement fabrics, therefore representing a coeval evolution between basement tectonic and sedimentation. Folding and faulting are ante-Permian, contemporaneous to postdating sedimentation (Toutin-Morin et al., 1994). East-West Permian grabens opening perpendicularly to the late-Variscan fabrics seal the MTM cycle (Fig. 1). These Permian intracontinental sediments and associated volcanics witness a short-lived rifting episode and are responsible for the Maures and Tanneron split in two distinct massifs (Toutin-Morin et al., 1994). Triassic continental deposits unconformably overlay the MTM and Permian sequence and mark the base of the thrusted Alpine-folded Mesozoic cover sequence that bounds the MTM to the North.

2.2 Eastern Tanneron massif

The study area is located in the Tanneron massif at the easternmost part of the MTM and belongs to the most internal domain of the belt (Fig. 1). The Tanneron massif is exposed along a 40 km E-W trending band bounded by the Mediterranean Sea and Permian deposits to the South, Alpine Mesozoic cover to the North and partially overlaid by the tertiary-quaternary Siagne alluvial deposits. This massif consists of a migmatised metasedimentary sequence with abundant metre to kilometre-long orthogneisses bodies (Crevola, 1977; Orsini, 1968) and host the carboniferous Reyran basin. Limited studies have focused on the Eastern Tanneron Massif, as such we present below lithological descriptions based on our personal field observations.

The migmatitic paragneisses are the dominant lithology of the area. They are dark stromatic metapelites (Fig. 2A) with a Qtz+Kfs+Pl±Bt±Ms±Chl assemblage with rare garnet, apatite, and tourmaline. Stable sillimanite and relictual kyanite can be found. Proportions of leucosome and melanosome are variable leading to different paragneiss facies but are still metatexites. They host lenses of orthogneiss, micaschist, layered amphibolite, quartzite, marble, and calc-silicate (Fig. 1).

The migmatitic orthogneisses are mica-bearing leucocratic orthogneisses (Fig. 2B) with rare thin leucosomes. Their granitic protolith was emplaced around 400 Ma (Oliot et al., 2015). Individual bodies are compositionally homogenous, showing a texture of regularly alternating stretched trails of dominant quartz-feldspars and trails of biotite-muscovite (Fig. 2B). In low strain zones, the granitoid protolith remains visible (Fig. 2C). Nevertheless, mineralogical variations are possible with several different facies and a diversity of fine variations is visible in the field between the orthogneiss and paragneiss, as already observed by Orsini (1968). The major difference between para- and orthogneiss seems to be the homogeneity at the outcrop scale, the orthogneiss showing constant distribution of mineral trails while paragneiss is made of alternating leucosome and melanosome bands varying in quantity and size.

To the East of the narrow Carboniferous Reyran basin, the leucocratic orthogneiss unit represents a long-stretched body inside the larger migmatitic paragneiss (Fig. 1). This unit is composed of a very fine grain highly stretched light gneiss, rich in quartz-feldspar with few muscovite and garnet which has been interpreted as a meta-rhyolite (Crevola, 1977; Orsini, 1968). Locally, different facies are associated with the leucocratic orthogneiss, mainly a darker medium grain orthogneiss.

Further East, the Cannes migmatites units are homogenous ortho-derived Qtz+Kfs+Pl+Bt±Ms pale pink to pale yellow migmatite with minor garnet and apatite (Fig. 2D). This ortho-migmatite is often micro-folded and shows thick coarse grain leucosomes with centimetric augen K-feldspar, alternating with thinner biotite-rich melanosomes (Fig. 2D). Stromatic migmatite fabrics are well preserved in this unit, with melts in leucosomes migrating toward the hinge of similar folds (Fig. 2E) and leucosomes injected in shear bands. Variations of the degree of anatexis in the migmatite create local secondary facies, such as nebulite (Fig. 2F).

Diverse granite and pegmatite veins emplaced within, or crosscutting the migmatitic foliation are widespread in the area, highlighting the partial melting of the crust in this internal part of the MTM. The Cannes migmatites are crosscut by sharp granite veins meaning that deep partial melting stands for a while until the end of the orogenic cycle.

Despite a polyphase tectonic history of the MTM during the Variscan orogeny, the protracted 325-300 Ma event has totally overprinted previous structures in the eastern Tanneron massif. Structural data remain scarce in the area, the main work was made by Crevola (1977) for the east of the Reyran basin (“oriental Tanneron”) which describe four deformation phases with a major pervasive “S2” N-S foliation defining large scale folds from the Reyran basin to the Cannes eastern termination. A kilometric synform with symmetric limbs on each side of the Reyran basin is followed by a large antiform with its eastern limbs ending around Cannes (Corsini et al., 2010; Crevola, 1977). Stretching lineations are gently plunging to the North or South (Crevola, 1977) and may be dominant over foliation locally to the west of the Reyran basin (Orsini, 1968). The area is also structured by the crustal La Moure SZ on the east-side of the Reyran basin which is a vertical dextral SZ (Rolland et al., 2009). Ar-Ar muscovite ages between 320-310 Ma in the eastern Tanneron are interpreted to represent this late structuration of the massif (Corsini et al., 2010).

3. Methodology

3.1 Field Mapping and Analysis

To investigate strain partitioning and evolution, we targeted two key zones for detailed field mapping and analysis: the Reyran zone and the Cannes zone. The Reyran zone, located on both sides of the Carboniferous Reyran basin (Fig. 1), represents a crucial transition between the coeval basin opening and ductile basement deformation. The Cannes zone, located at the extreme east of the massif (Fig. 1), represents the innermost part of the orogen, with ubiquitous migmatites displaying high-temperature fabrics. Exposure in this latter is separated into three close hills: the Roquette-sur-Siagne hill, the Croix des gardes hill, and the Super-Cannes hill (Fig. 1). Both key areas were thoroughly investigated and sampled with the acquisition of more than 4500 structural measurements. Field observations and measurements were acquired through digital mapping on an iPad-mini tablet with FieldMove software (Midland Valley). Observations and direct measurements were exported to a GIS software for data analysis and interpretation, and thematic map building. For each outcrop, foliation and/or lineation were systematically measured, and a qualitative estimate of the finite strain ellipsoid shape was given in the form of a tectonite classification scheme (S>L, S-L, L>S-tectonite) when outcrop quality was sufficient (see §3.2 below).

3.2 Qualitative method: Tectonite-Type Map

We built a qualitative tectonite-type map (see §4.4) showing three different symbologies corresponding to S>L, S-L, and L>S tectonites. For most outcrops, the tectonite type was gauged from direct field observations of the fabrics geometry between the XZ and YZ planes. For others, tectonite type was attributed directly on GIS software following this classification: Outcrops where only a flattening plane foliation was identified and measured have been classified as S>L, outcrops where both a foliation and mineral or stretching lineation was identified have been classified as S-L, and outcrops where only mineral or stretching lineation was identified have been classified as L>S.

3.3 Quantitative Methods: Microstructural Ellipses Measurement and Anisotropy of Magnetic Susceptibility (AMS)

To validate the qualitative observations, we used two quantitative methods: microstructural ellipses measurement and anisotropy of magnetic susceptibility

(AMS). 3D finite strain ellipsoids were calculated based on microstructure observations for 20 oriented samples. These samples were cut along and across the main foliation and/or lineation in order to produce two thin sections parallel (XZ plane) and perpendicular (YZ plane) to the principal finite strain axis. We acquired high-resolution scans of the whole thin sections. Then, we used EllipseFit software version 3.8.2 (Vollmer, 2018) to calculate statistical ellipsoid parameters from ellipses drawing. The Fry technique was not used because Fry's starting hypothesis implies that the reference objects were of the same size and homogenously distributed before deformation. In the migmatitic units, leucosomes were often targeted as reference objects because of their homogenous composition and as they represent a good marker of finite deformation of the rocks in sub and supra-solidus conditions. Mean ellipses factors were obtained by digitising polygonal shape of leucosomes on thin section scans then converted to an ellipse with the "Shape" method of EllipseFit. After that, the mean 2D ellipse factors from thin sections parallel and perpendicular to the stretching axis are gathered to reconstitute the mean 3D ellipsoid factors of the sample with the Shan method (Shan, 2008). Resulting ellipsoid parameters are compiled (Table 1) and plotted in a Flinn diagram to visualise the shape and intensity of finite strain for each sample.

For the magnetic fabric study, 75 oriented cores were sampled using a gasoline-powered portable drill at 5 sampling sites in paragneiss and orthogneiss of the Reyran zone. Four sites follow a broad E-W cross-section in the La Moure SZ and one site is located in the major orthogneiss body of the west side of the Reyran basin. The cores were cut in the laboratory (see below) in specimens of standard paleomagnetic size. The AMS was measured using a MKF1 Kappabridge at the University of Saint Etienne, LGL-TPE laboratory (France) and data were processed from the ANISOFT package of programs (AGICO, Inc). Coupling a CS4 furnace to the MFK1 Kappabridge allowed conduct thermomagnetic measurements to precise the magnetic mineralogy. The AMS data are represented by three main parameters namely Km, Pj, and T. The Km parameter is defined by Km= (K1+K2+K3)/3 as the mean bulk magnetic susceptibility, where K1 ≥ K2 ≥ K3 are the three principal susceptibility axes of the AMS ellipsoid. Following the magnetic fabric, K1 (Kmax) depicts magnetic lineation and K3 (Kmin) denotes a pole to magnetic foliation. The Pj parameter is the corrected anisotropy degree and represents the intensity of the magnetic fabric which reflects the eccentricity of the AMS ellipsoid. The T parameter of Jelinek (1981) defines the shape of the AMS ellipsoid, which ranges between -1 (prolate ellipsoid) and 1 (oblate ellipsoid).

4. Structural architecture and strain pattern

4.1 Planar fabrics

Planar deformation pattern is separated in 2 sets of fabrics, a low strain sub-horizontal S2a foliation and a higher strain sub-vertical S2b foliation (Fig. 1 and 3). Although a former S1 foliation is evidenced by the preservation of seldom folds with axial planes parallel to the S2a foliation, its continuity cannot be mapped in such migmatite terrains. The S2a fabric is approximately E-W trending and dips gently (0-40°) to the North in the Cannes zone and to the South in the Reyran zone (Fig. 4A). Yet, kinematic indicators both to the East and West generally highlight top-to-the-South movements (Fig. 4B). However, asymmetric criteria are scarce and fabrics are mainly coaxial pointing to a dominant pure shear kinematic. Despite an overall E-W strike, the S2a foliation shows local variations due to late folding which are represented by small irregular curves on the foliation trajectory (Fig. 3). The S2a trend direction is not well constrained on the south-western part of the Reyran zone and in some part of the Croix des Gardes hill because foliations are missing and only lineations are measurable. Around the Reyran basin S2a is restricted to narrow preserved patches surrounded by anastomosed corridors with S2b foliation (Fig. 3A). S2a is more visible in the Cannes migmatites and orthogneiss lithologies than in the paragneiss. In the Cannes zone, S2a is well developed and predominant among the S2b. The Super-Cannes hill (Fig. 3D) is mostly defined by gently dipping S2a foliations (0 to 20˚) (Fig. 4A) and exhibits complex foliation patterns with a vague NW-SE trend locally deflected by hectometric domal shapes at the origin of triple junctions causing high variability of trending directions. The main striking direction is approximately NW-SE but E-W as well as N-S and NE-SW directions are also observed (Fig. 3B). These heterogeneous trending directions are highlighted by foliation triple points and a concentric half-dome structure in the west part of the hill. S2a foliation is overprinted by the S2b vertical foliation as illustrated by the S2a deflection at the contact with the La Moure SZ, especially in the south of the SZ (Fig. 3A). Locally, S2a foliation is folded and transposed along subvertical S2b planes (Fig. 4C).

Although S2b foliation is pervasive in the whole study area, it is far better developed in paragneisses than in orthogneisses or in the Cannes migmatites. S2b foliation trends N000 to N020 with sub-vertical (60-90°) dips (Fig. 3) and its occurrence is associated with high strain zones defined by SL fabrics. This plane strain deformation is associated with strike slip kinematics forming widespread metric to kilometric SZ especially concentrated to the eastern side of the Reyran basin. The major La Moure SZ is the biggest and most representative of those. This latter consists in a 1 km wide anastomosed network of vertical foliation bounding the eastern side of the Reyran carboniferous basin along a roughly N015-020 trend (Fig. 3A). There, mylonitic paragneiss has a dark recrystallised fine grain matrix into which sheared leucosomes are transformed into disrupted and stretched lenses or separated in trails of clasts (Fig. 4D). Ultramylonite of the paragneiss are also visible with >90% recrystallised matrix and millimetric-to-centimetric rounded pearls of leucosomes. The main kinematic of the La Moure SZ is dextral (Fig. 3) which is visible through a majority of dextral S/C structures, asymmetric leucosome sigmoids, drag folds, and mica fish (Fig. 4E,F). Sinistral indicators are also present locally. Deflection of the S2a foliation against the La Moure SZ also indicates mostly sinistral kinematic (Fig. 3). Previous authors describe complex kinematics for the main transcurrent SZ of the MTM and Sardinia, and suggest successive phases of dextral and sinistral kinematic (Bellot, 2005; Buscail, 2000; Carosi et al., 2012; Vauchez and Bufalo, 1988). From East to West a strain gradient is visible inside the La Moure SZ evolving from mylonite to ultramylonite near the Reyran basin border. Ultramylonite on the edge of the basin are often also deformed under brittle conditions showing fracture network. In the Cannes zone, the S2b foliation is distributed in small scattered N-S vertical corridors inside the dominant E-W S2a foliation.

The entire structure is folded (in association with the development of S2a and S2b foliations) from the centimetric to decametric scale depending on the lithological units. The Cannes migmatites are highly micro-folded (Fig. 5A) and show regular metric to decametric cascading folds (Fig. 5B) while other units appear less folded and show mainly localised decimetric folds. In all the area, folds are gently plunging between 10 to 30°, to the North in the Cannes zone (N340-020) and to the South in the Reyran zone (N180-210), being parallel to the local stretching lineation (L2) which is a common feature of oblique tectonics (Fig. 6). Few steeply dipping fold axes plunging around 60-70° are also visible locally in the Croix des Gardes hill and Reyran zone. Axial planes are mainly parallel to the surrounding foliation, and therefore follow directions close to E-W in S2a foliation domain whereas the axial planes trend close to N-S in S2b foliation domain. In the Reyran zone folds are close to tight, most of the time symmetric and concentric whereas folds in the Cannes zone are more diversified and disorganised. Most of the micro-folded structures in the Cannes zone are close to tight and symmetric but decimetric to metric folds show also gentle to open folds, and asymmetric and/or similar folds. Some of these gentle to open folds are not considered as tectonic but attributed to the natural buoyant flow of this migmatitic hot and soft unit.

4.2 Linear fabrics

Mineral and stretching lineations L2 are ubiquitous and represent a major feature of the structural pattern of the Tanneron Massif. Stretching lineations (L2) are represented by stretched leucosomes (and melanosomes), elongated quartz rods, and micas trails. Unlike planar fabrics, lineations (L2) set a homogenous and consistent structural pattern through the whole area. This is a common feature through all the MTM, at least for the internal domain of the Maures massif (Bolle and al., 2023). Thus, the lineations (L2) form a single set and are systematically associated with both S2a and S2b foliations. Linear fabrics L2 are described by N-

S directed sub-horizontal stretching lineations dipping mainly between 10 to 30° (Fig. 6). The stretching lineations field transcend continuously all the lithological units without variation through lithological contacts showing that the entire area was deformed in the same tectonic regime. The plunge direction changes between North and South from East to West respectively (Fig. 6). In detail, plunge directions are ranging between N340-N030 in the eastern part and N230-N160 in the western part of the study area, and show curved trajectories that converge or diverge (Fig. 6). Lineation (L2) at high angle to the mean N-S directions can be seen locally in the west and east of the Reyran basin, with N240-250 directions. Around the Reyran basin, lineations are mostly oblique to the La Moure SZ, which represents the reference for simple shear flow. In fact, the main direction of the La Moure SZ is N015-020 while lineations (L2) follow two main directions, N220 and N165, giving mean angles of 20-30° between the SZ and the lineation.

In many places lineation (L2) is the main structural feature defining the rock fabric and outcrop architecture. Usually, stretching lineation presents a dominant continuous direction while foliations are much more variable, with their strike and dip evolving by folding around the axis of the lineation. The predominance of stretching lineations (L2) over flattening foliation planes is visible in these rocks until the development of L>S tectonites. In fact, especially away from the S2b corridors, it is common to find outcrops where foliation is weak to non-recognisable compared to the sturdy stretching lineation (L2) up to the point when only lineation is visible (Fig. 5C,D). In three dimensions at outcrop scale as well as in thin section, these L>S tectonites present cigar-shape with leucosomes trails or quartz rods highly elongated in the XZ section and rounded in the perpendicular YZ section (Fig. 5D and E-F).

4.3 Finite strain shape

The major sub-horizontal to gently dipping stretching flow in the area leads to the development of L>S and subordinate S-L tectonites more than S>L-tectonites (Fig. 7). Flattening strain is mostly restricted to the Super-Cannes hill (Cannes migmatite unit) where the flat-lying foliations are frequently seen without any associated lineation and show similar deformation degree between the XZ and YZ planes (Figure 4B and 7). S-L-tectonites, representing plane strain fabrics, are widespread in the whole area and mainly along the S2b sub-vertical foliation, especially inside the La Moure SZ (Fig. 3 and 7). Constriction (L>S type tectonite), following the gently dipping lineation (L2) direction, is very common but is more prevalent in the E-W S2a foliation zones. Constriction is mostly visible in the orthogneiss units and the Croix des Gardes and Roquette hills of the Cannes migmatite (Fig. 7) suggesting a lithological control for the preservation of such fabric. In the field, these areas are marked by the occurrence of L-type tectonites displaying spectacular leucosomes rods, highly stretched along the X-axis and wrapped around by micas along the orthogonal YZ plane (Fig. 5C,D). On this YZ plane, no consistent foliation is observed. The various meta-igneous units set a remarkable contrast with the migmatitic paragneiss. In fact, the transition between migmatitic ortho- and paragneiss is instantly marked by the appearance of a highly developed stretching lineation (L2) compared to foliation.

In order to confirm these macroscopic observations, finite strain ellipsoids were measured through microstructural analysis on 20 samples (Table 1, *see Methodology section*). Results for each sample are following the apparent finite strain shape of the field (Fig. 7) and the same structure are observed. The L-tectonite defined the same elongated quartzo-feldspathic or mica trails along the XZ plane while no clear orientation is visible in the YZ plane showing only rounded quartz/feldspars surrounded by micas (Fig. 5E,F). Results are also compiled in a Flinn diagram which highlights a link between lithology and finite strain ellipsoid shape (Fig. 8). Indeed, the paragneiss samples plot along the plane strain line (k=1) while most of the migmatitic orthogneisses and Cannes migmatites are gathered in the constriction field (k>>1). Mylonite samples JG20-01/JG20-02/JG21-05A from the La Moure SZ plot close to the plane strain line supporting a simple shear flow for this strike slip SZ. Only one sample is located in the flattening field, demonstrating the monotony of the strong L>S and S-L tectonites which point to a rather homogenous deformation pattern in the complete area.

4.4 Magnetic fabric parameters and orientation (AMS)

The anisotropy of magnetic susceptibility (AMS) was carried on three paragneiss sites namely TR1, TR2, JG20-06 and two orthogneiss named JG20-05 and JG21-02 (Fig. 9). Sites JG20-05/JG20-06/JG21-02 belong to the same sampling sites as the corresponding sample names used for microstructural ellipses measurement (Table 1). All analysed sites show a very good concordance between structural data measured in the field and the magnetic foliations and lineations (Fig. 9). This suggests that magnetic minerals were deformed during the same tectonic event than the dominant quartzo-feldspathic phases and led us to analyse the potential contribution of other AMS parameters such as magnetic anisotropy degree (Pj) and shape parameter (T).

For sites TR1 (paragneiss)/JG20-05 (orthogneiss)/JG21-02 (orthogneiss) the bulk magnetic susceptibility (Km) varies between 50 and 270x10^{-6} [SI] (Fig. 9), which is lower than the cutoff point of 500x10^{-6} [SI] below which suggest that the rock magnetic susceptibility is mainly carried by paramagnetic minerals (Bouchez, 2000; Rochette, 1987). Other observations (reflected-light microscopy, thermomagnetic curves and Km-Pj plots analyses (Fig. 9) are consistent with a paramagnetic contribution for the rocks magnetic susceptibility. Petrological thin-section studies show that biotite and muscovite are the dominant paramagnetic minerals and biotite is always present in higher proportion than muscovite. Thus, biotite is expected to be the major contributor to the magnetic susceptibility in these sites. The Jelinek plot (Pj vs T) for these three sites gives values between -0.3

to 0.5 indicating that the T parameter plot mainly around 0 in the plane strain domain (Fig. 9). This is in agreement with the observed SL tectonic style for TR1 (paragneiss) (Fig. 7) but not for the L tectonites described for JG20-05 and JG21-02 (orthogneisses). Conversely, finite strain ellipsoid calculation has also confirmed the prolate strain shape of both sites (Fig. 8).

Km values of sites TR2 and JG20-06 (paragneisses) range from approximately 300 - 3000x10-6 [SI] being largely higher than other sites. TR2 shows a prominent linear correlation between Km and Pj (Fig. 9) with Km values ranging from 350 to 2600x10-6 [SI]. Such correlation associated with a mean magnetic susceptibility higher than 500x10-6 [SI] indicates the ferromagnetic contribution, especially magnetite reference (Henry et al. 2004; Rochette, 1987). Reflected-light microscopy and thermomagnetic curves analyses confirm the magnetite presence. The Jelinek plot of site TR2 reveals a mean plane strain shape for the AMS ellipsoid (Fig. 9) in agreement with the observed SL tectonites in the field (Fig. 7). The bulk magnetic susceptibility (Km) values of site JG20-06 are divided into a tightly clustered group of 300 - 400x10-6 [SI] and a broader one around 900 - 1300x10-6 [SI] with a slight linear correlation between Km and Pj (Fig. 9). In view of the site petrography, the low K group below 500x10-6 [SI] is more likely to be rich in biotite and the higher K group with ferromagnetic minerals. Each group gives a different ellipsoid shape in the Jelinek plot (Fig. 9), biotite plot in the oblate domain while ferromagnetic minerals have value in the oblate and plane strain domain. This is also visible with site TR2 where the only two measurements with a bulk susceptibility lower than 500x10-6 [SI] in the Km-Pj plot, have also the highest T value in the Pj vs T plot, getting closer with the oblate shape domain. Both mineralogic groups of JG20-06 are broadly in agreement with the observed S>L tectonites on the field (Fig. 7) and the oblate finite strain ellipsoid shape of JG20-06 plot in the Flinn diagram (Fig. 8).

4.5 Deformation temperature

Microstructural observations are used to constrain the relative deformation temperature across the area. Rocks of the eastern Tanneron massif display a diversity of microstructures (Fig. 10) during progressive retrogression from high temperature suprasolidus fabrics down to subsolidus low temperature brittle-ductile fabrics.

High temperature conditions are inferred for the Cannes migmatite unit (which are mainly related to S2a foliation). These migmatites are composed of Qtz + Kfs + Pl + Bt + Ms ± Grt with no chlorite, unlike other units. The texture is defined by homogenous large quartz and feldspar grains (0.5-1.5 mm) aligned parallel to the lineation (L2) in the foliation which is typical of high-T regime (Fig. 10A) (Gapais, 1989). Some key microstructures indicative of melt-present deformation are recognised such as small dihedral angles of interstitial phases, interstitial quartz melt infilling pore space, and elongated interstitial quartz and feldspar grains (Lee et al., 2018; Roberts and Tikoff, 2021; Stuart et al., 2018; Zibra et al., 2012). In addition, feldspar and quartz dynamic recrystallisation also indicates high-T deformation (Roberts and Tikoff, 2021). Quartz exhibits typical grain boundary migration (GBM) with irregular and amoeboid boundaries (Fig. 10A) that are considered to reflect temperature higher than 550°C (Stipp et al., 2002). However, it is important to keep in mind that quartz dynamic recrystallisation is also dependent on strain rate.

Orthogneiss units (which are mainly related to S2a foliation) are also characterised by the presence of small dihedral angles of interstitial phases, interstitial quartz melt infilling pore space, and myrmekite around large K-feldspar, indicating the former presence of melt during the onset of deformation (Lee et al., 2018; Roberts and Tikoff, 2021; Stuart et al., 2018; Zibra et al., 2012). But compared to the Cannes migmatite, orthogneiss have a heterogeneous smaller grain size (0.3-1mm) and discrete highly recrystallised shear bands which emphasise also lower temperature condition with subsolidus deformation (Fig. 10B). Indeed, during the progressive evolution from suprasolidus to low grade (400-500°C) deformation, homogenous penetrative foliation evolved to heterogenous localised high strain shear bands showing a significant grain size reduction through dynamic recrystallisation (Ebert et al., 2007; Fossen, 2017; Gapais, 1989). Quartz dynamic recrystallisation is visible through HT GBM (Fig. 10B) and also with few evidence of lower temperature subgrain rotation (SGR). Biotite and muscovite are recrystallised into smaller grains only within local shear bands. Some orthogneiss are composed of rare biotite transformed into chlorite.

Migmatitic paragneiss are composed in majority of Qtz + Kfs + Bt + Ms with a variable proportion of chlorite, up to 10% of the modal composition, and rare sillimanite. These paragneiss (which are mainly related to S2b foliation) have generally mylonitic textures with anastomosed shear bands around low strain domains or pervasive S/C structures, typical of amphibolite to greenschist facies deformation (Fossen, 2017; Gapais, 1989). Grain size is significantly lower (0.2-0.5 mm) than in the Cannes migmatites or the orthogneiss and can be very heterogeneous with large preserved grains from the early HT fabric (1-2 mm) wrapped around by the main fine grain sheared matrix (0.1-0.2 mm). Biotite and muscovite are highly recrystallised into micrometric grains inside the mylonitic matrix while quartz is mainly recrystallised by SGR and shows preserved GBM textures or even few low temperature bulging (BLG). Biotite and chlorite are in inter-boudin growth position or inside shear bands indicating syn-kinematic development. Hence, the widespread shear bands development, grain size reduction, SGR/BLG textures and the significant chlorite amount point to a medium to low temperature deformation in the presence of fluids from lower amphibolite to greenschist facies conditions. In addition, several preserved textures indicate a former HT deformation: small dihedral angles of interstitial phases (Stuart et al., 2018), quartz dynamic recrystallisation through GBM, ductilely deformed feldspar, and the presence of sillimanite in the melanosome. Inside the La Moure SZ, an increasing strain gradient accompanied by a decreasing deformation temperature closer to the Reyran basin border may be inferred from microstructure analysis. Migmatitic paragneiss close to the Reyran basin border show a higher grain size reduction and brittle-ductile shear bands development than others and are characterised by SGR and few BLG quartz recrystallisation while eastern migmatitic paragneiss of the shear zone preserved more GBM textures. These low grade ultramylonites derived from the migmatitic paragneiss are mostly localised on the border of the Reyran basin but the strong spatial variation of the chlorite proportion makes it impossible to map this ultramylonite as a separate unit, and the intense weathering of the basement giving wrong impression of changes leads us to avoid this term.

Deformation temperature inferred by microstructures study emphasises a cooling gradient during deformation from East to West in the area. Indeed, the Cannes migmatites are described by HT fabrics with a main suprasolidus deformation while orthogneiss and paragneiss show microstructures indicative of subsolidus deformation until low-T conditions near the brittle-ductile transition along the Reyran basin border. Interestingly, all units are characterised by the presence of preserved microstructures designating suprasolidus deformation. In detail, microstructures also reveal contrasting deformation temperature between meta-igneous and meta-sedimentary rocks with the Cannes migmatites and migmatitic orthogneiss being deformed at suprasolidus and/or high temperature subsolidus conditions while migmatitic paragneiss show few early HT deformation textures subsequently overprinted by dominant medium to low-temperature fabrics. Because S2a foliations are more developed in the Cannes migmatite and orthogneiss unit and S2b foliation in the paragneiss unit, this means that deformation temperature was higher for the S2a fabric than S2b fabric.

5. Discussion

5.1 Origin of the cryptic Cannes structure

The Cannes migmatites exhibit a complex structure, highlighted by distinct differences between the Croix des Gardes and Super-Cannes hills. In the Croix des Gardes area, constrictional flow with strongly deformed L>S tectonites is prevalent, and defines the rock architecture (Figs. 5 and 7). In contrast, the Super-Cannes sector displays flattening strain on mainly seldom deformed sub-horizontal foliations (Figs. 4 and 7). The Croix des Gardes hill is defined by monotonous E-W striking S2a, locally reworked by N-S S2b, while the Super-Cannes hill presents a more chaotic pattern of S2a (Fig. 3). The latter exhibits a folded structure with numerous changing directions, emphasised by foliation triple points and a sub-dome structure in the western part. Despite these differences, both areas share a common lineation pattern, with stretching lineations (L2) consistently plunging between N000-N020°, indicating the need for integration within the same global framework.

The preserved migmatitic nature of the Cannes migmatite unit (Fig. 2E, F) through suprasolidus deformation structure suggests two possible models to explain the observed architecture: a tectonic dominated model and a buoyancy-isostasy dominated model (Kruckenberg et al., 2011). The tectonic dominated model implies that constrictional and flattening fabrics from each sector must be kinematically consistent in the same strain regime, which appears conflicting. Additionally, the sub-dome concentric foliations orientations and foliations deflection around triple points are challenging to reconcile with a common kinematic regime. Conversely, buoyancy-isostasy driven flow, as documented for diapirism (Dixon, 1975; Cruden, 1990), can explain the highly variable orientation of flattening fabrics. Diapirism also predicts the coexistence of flattening and constrictional fabrics, with constriction expected in the core of a rising diapir and flattening around the outside and the top (Cruden, 1988, 1990; Sullivan, 2013; Talbot and Jackson, 1987).

In hot orogens with buoyant lithosphere, field-based structural studies have demonstrated that flat fabrics in lower crustal levels may consist of vertically shortened and horizontally sheared roofs of domes (Dirks et al., 1997; Gapais et al., 2005, 2008; Gébelin et al., 2006). In this scenario, the Croix des Gardes hill could represent the inclined diapir center, and Super-Cannes the flattened outside.

Alternatively, a third option to explain these contrasting structures could involve variations in the exposed structural level, with Croix des Gardes as a diapir core caracterised by constriction and Super-Cannes as a diapir roof caracterised by flattening. In this model, the migmatite dome is divided into several N-S directed inclined subdomes with axes following the stretching lineation, where each hill represents a different diapir.

Gravity-driven flow is a plausible process to account for some structural features within the Cannes migmatite unit. However, the continuous lineation field (L2) between both areas and the presence of S2b vertical foliation zones cannot be fully explained by gravity-dominated forces alone. Foliations wrapping around the average lineation direction, a common tectonic feature of syn-tectonic domes (Darrozes et al., 1994; Djouadi et al., 1997; Nédélec et al., 2015), are also recognised in the field (Fig. 5A-B) and documented in this study (Super-Cannes hill stereograms: Fig. 3 and 6). These observations suggest that flow within the migmatitic unit was controlled by a combination of independent internal gravity forces and a strong oblique tectonic framework. Elongated migmatitic domes parallel to the stretching direction can form in zones of local horizontal flow within a transtensive regime (Denèl et al., 2017; Le Pourhiet et al., 2012; Rey et al., 2017).

The Super Cannes hill, representing a tectonically preserved area, is dominated by high-temperature structures related to internal buoyancy-driven flow rather than tectonic forces. This is supported by its specific eastern location, representing the most internal part of the unit, combined with the greater presence of nebulitic facies and lower strain migmatites (Fig. 2E,F). In contrast, the presence of strongly stretched L-tectonites and S2b vertical foliations at the Croix des Gardes and Roquette hills indicates an increasing influence of tectonic forces when moving westward in the massif.

5.2 Lithological control on finite strain ellipsoid measurements

Finite strain analyses reveal contrasting ellipsoid shapes between different lithologies. Paragneiss lithology is mainly associated with S-L tectonite on the map scale (Fig. 7) and plots along the plane strain line (Fig. 8), while Cannes migmatites and orthogneiss units are characterised by numerous L>S tectonites (Fig. 7) and fall within the constrictional field of the Flinn diagram (Fig. 8). This contrast is evident in the field, where transitions between these lithologies often exhibit a sharp change marked by the appearance of strong stretching lineations (L2) and L>S tectonites. Phyllosilicates-rich paragneiss units, derived from meta-sedimentary series, are considered rheologically weaker than orthogneiss and Cannes migmatites. This suggests that heterogeneous and weaker lithologies display more evidence for plane strain deformation, while homogenous and stronger lithologies are characterised by constrictional strain deformation.

Rheologically driven strain path partitioning, with the concentration of L-type tectonite in stronger homogenous units, has been described in previous studies (Fletcher and Bartley, 1994; Sullivan, 2006, 2008, 2013) and partitioning of non-coaxial deformation into rheologically weak domains, such as schist units, is predicted by many field observations, theoretical studies and numerical simulations (Goodwin and Tikoff, 2002; Goodwin and Williams, 1996; Jiang, 1994a, b; Lister and Williams, 1983; Sullivan, 2008, 2013). Thus, we propose two potential scenarios to explain this rheology-dependent finite strain shape variation: strain path partitioning with each lithology accommodating a single deformation phase differently, or each lithology recording different deformation phases. The consistent structural lineation (L2) field transcending all lithologies and widespread folding of most units with axes parallel to this stretching lineation (L2) support strain partitioning during a single deformation phase. However, several factors suggest that the observed rheologically driven finite strain shape contrast is caused by differential recording of two deformation phases during a progressive deformation event.

First, L>S tectonite types inside meta-igneous units are mostly associated with the low-strain and high-T S2a foliation, which is primarily confined to these lithologies, while high-strain medium to low-T S2b foliations are mainly visible in the paragneiss unit defined by S-L tectonite. Second, S2a foliations are transposed and overprinted by S2b foliations, highlighting a deformation chronology (Fig. 3). Finally, microstructure analyses reveal that deformation in meta-igneous units occurred at higher temperatures than in the meta-sediment units (Fig. 10). Thus, we suggest that the constrictional flow and associated S2a foliations were formed during a first deformation phase, subsequently overprinted by a second phase represented by S2b foliations.

Contrary to expectations, meta-sedimentary units which are mainly deformed by high strain S2b foliation and associated SZ do not plot in higher deformation domains than meta-igneous units in the Flinn diagram, and the opposite is even observed (Fig. 8). In fact, the leucosomes and/or quartz layers chosen as reference material for ellipses calculation were too much sheared until being recrystallised in smaller lenses and clasts during the second phase, erasing their stretched shape from the first phase. High strain deformation mechanisms at middle to low temperature tend to reduce grain size and spread-out former fabrics (Ebert et al., 2007; Fossen and Cavalcante, 2017; Gapais, 1989), which could lead to minimising finite strain intensity with the ellipses method used in this study.

The magnetic foliation and lineation of each site are in the same range as structural measurements in the field. The orientation of the principal axes (Kmax, Kint, Kmin) from AMS measurements could therefore provide a valuable complement to field measurements. However, the use of AMS to quantify finite strain and study the shape of the finite strain ellipsoid remains limited, as pointed out by various authors (e.g., Borradaile and Henry, 1997; Borradaile and Jackson

2010). AMS combines contributions from all magnetic minerals (diamagnetic, paramagnetic and ferromagnetic) which could develop distinct magnetic fabrics.

The AMS ellipsoid shape for sites of low magnetic susceptibility values with a magnetic mineralogy dominated by paramagnetic minerals, in particular biotite give opposite results to observed and measured finite strain ellipsoids for strong L-tectonites (JG20-05 and JG21-02, Fig. 9). The shape anisotropy of micas is known to generate generally oblate AMS ellipsoid (Rochette et al., 1992) which is well illustrated by site TR2 and JG20-06 in which measurements attributed to paramagnetic biotite give more oblate values than those from ferromagnetic minerals in the same rock (Fig. 9). The observed poor correlation between the shape of AMS and finite strain ellipsoids for constrictional strain in this study was already reported in previous studies where oblate AMS ellipsoids were obtained from L>S tectonite in gneiss with a magnetic susceptibility controlled by micas (Das et al., 2021; Skytta et al., 2010).

Conversely, AMS sites richer in ferromagnetic minerals (TR2 and JG20-06) provide a good correlation with observed and measured finite strain ellipsoids (Fig. 9). This good agreement could be due to the presence of magnetite which is characterised by a grain-shape alignment anisotropy (Borradaile and Henry, 1997; Borradaile and Jackson 2010; Ferré et al., 2014). The determination of the sub-fabric carried by the ferromagnetic minerals by using magnetic remanence anisotropy techniques for example (Hrouda, 2002; Jackson, 1991) could better constrain and use the AMS measurements.

5.3 Transpression vs transtension?

The internal part of the Maures-Tanneron massif aligns with an oblique tectonic framework, particularly due to the vertical shear zone's strike-slip component associated with shallowly plunging lineation, which trends at a low angle to the shear's strike. Fold axes parallel to the regional lineation (L2) are another common feature of oblique tectonic systems (Fossen et al., 1994, 2013). A transpressional tectonic setting was previously proposed by Rolland et al. (2009), based on the observation of a dome structure around the Rouet granitic intrusion and N-S kilometer-scale folds defining the structure of the Tanneron massif, following the previous interpretation made by Crevola (1977). This transpression context is inferred for the entire Maures-Tanneron massif. However, in the eastern Tanneron, representing the more internal part of the massif, our results point to a transtensional event. The kilometer-scale folds described by Crevola (1977) (and after Rolland et al., 2009) are not observed, and we identify two sets of planar fabric with a main S2b vertical foliation. Moreover, numerous folds of different geometries are visible in the field, but they do not necessarily indicate a convergence context, as folds can form readily during transtension (Fossen et al., 2013), or progressive constrictional strain as experimentally demonstrated by

Ghosh et al. (1995). Analytical models (Fossen and Tikoff, 1993; Fossen et al., 1994, 2013) demonstrate that fold axes evolve from vertical to horizontal plunge during transtension while the opposite is predicted for transpression, and fold axis direction tends to rotate parallel to the SZ boundary for transpression while retaining angle of 10-15° even for simple shear dominated transtension (Fossen et al., 2013). Here, fold axes have a mean 10-30° plunge and directions follow the lineation (L2), which mainly strike at an angle of 20-30° to the La Moure SZ reference. Therefore, fold axis directions and plunges match characteristics of transtensional folds more than transpressional folds. Additionally, stretching lineation parallel to fold axes is seen as a signature of transtension at the middle-lower crust level (Fossen et al., 2013) and transtensional folds are often associated with constrictional strain and large magnitude stretching, which aligns with our data.

Various analytical models have studied oblique tectonics through different combinations of pure and simple shear applied to a deforming volume stuck between rigid boundaries (Dewey et al., 1998; Fossen and Tikoff, 1993, 1998; Jones et al., 2004; Sanderson and Marchini, 1984). In terms of strain, all models show that transpression develops flattening strain, whereas transtension favours constrictional strain. In the Tanneron massif, finite strain shape analysis supports the widespread gently dipping constrictional flow, indicating the importance of L and L>S tectonites (Fig. 7 and 8). L or L>S tectonites are predicted within the Flinn diagram as a common feature for transtension, with associated well-developed lineations remaining oblique to the shear direction (Fossen and Cavalcante, 2017; Sanderson and Marchini, 1984). This is in agreement with the lineation field (L2) of the area remaining mainly oblique to the shear direction (20-30°) (Fig. 6). Various analytical graphs developed in Fossen et al. (2013) could be used combining ellipsoid principal strain axes or folds tightness data and/or angles with the SZ to decipher between transpression and transtension regime and obtain theoretical dynamic vorticity Wk values for the subsimple shear deformation. In our data, the length of minimum horizontal principal strain axis (Z or Y) ranges between 0.67 and 0.32 with a mean 0.52 value and the length of maximal horizontal principal strain axis (X) between 1.38 and 3.90 with an average 2.54 value. Folds in the area are mostly close to tight matching the corresponding range of Z axis length as proposed by Fossen et al. (2013). Assuming an average angle of 20-30° between the lineation (L2) and SZ, graphs comparing this angle with length of principal strain axis (X or Z) give mainly values close to the simple shear curve which plot in majority in the simple shear dominated transtension (Fossen et al., 2013 fig 4 and 7). Wk ranges between 0.8 and 1 highlighting the important simple shear flow. The X axis vs Z axis plot also provides a majority of data in the simple shear dominated transtension with vorticity ranging between 0.8 and 1 and a 0.95 Wk by considering the mean values for length of X and Z axes (Fossen et al., 2013 fig 8). These high vorticity numbers are in agreement with the predicted rotation of folds, requiring a minimum Wk of 0.7 to obtain fold axes with angle of 20-30° to the SZ, as observed in the area (Fossen et al., 2013 fig 5). Theoretical $\boldsymbol{\gamma}$ gamma values of the shear strain are also provided in these graphs and stand approximately between 1.5 and 2.5 which emphasised the high strain deformation in these late transtensional regime.

The combination of constrictional strain and domes representing the pure shear component and S-L tectonites through strike-slip SZ representing the simple shear suggests a general transtensional tectonic framework in the Tanneron massif. This regime manifests during the late-stage evolution of the massif between 320-300 Ma, associated with an oblique collapse of a hot crust. In the internal part of the Maures massif, a strong longitudinal horizontal crustal flow was recently highlighted by the predominance of subhorizontal stretching lineations, striking continuously N-S through the migmatitic basement (Bolle and al., 2023). These authors suggest that this subhorizontal extension associated with strike slip SZ induced thinning of the continental crust associated with partial melting, granitic intrusions and exhumation of the lower continental crust during the latest event of the belt (325-298 Ma). In addition, late dextral shear-zones developed from near-solidus amphibolite metamorphic facies down to brittle-ductile conditions are described in the MTM (Simonetti et al., 2020) and Corsica-Sardinia block (Frassi et al., 2009; Giacomini et al., 2008), which agree with our description of the second phase and the development of the La Moure SZ.

A key element is the opening of the Reyran Carboniferous basin, which strikes parallel to the surrounding La Moure SZ (N10-20) (Fig. 3). This pull-apart basin is thought to have opened around 310-300 Ma (Toutin-Morin et al., 1994), roughly synchronous with the end of the basement oblique tectonic event. The nearby La Moure SZ and the basin's particular shape, which might be seen as four former NE-SW en-echelon sub-basins (Fig. 1), support the opening being caused by an oblique tectonic regime. Moreover, carboniferous sediments are strongly folded in specific sectors, suggesting potential syn-sedimentary deformation (Maillet, 2021). In this context, the opening of this type of basin is more likely in a transtensional regime because the stretching component of transtension contributes to thinning the crust, contrary to the vertical flattening strain developed by transpression. In the Variscan belt, the opening of a pull-apart basin during a dextral transtensional regime between 315-300 Ma was also described in the Montagne noire (Chardon et al., 2020; Franke et al., 2011; Rey et al., 2017).

5.4 Progressive deformation and strain partitioning during exhumation

In our structural analysis, we identified two distinct strain patterns and divided planar fabrics into two sets: an E-W flat lying S2a foliation and a N-S vertical S2b foliation (Fig. 3). The S2a foliation is primarily observed in the Cannes migmatites and orthogneiss unit, while the S2b foliation is more prevalent in the paragneiss unit. Finite strain shape ellipsoids are also grouped according to lithological units, with prolate strain associated with ortho-derived units and plane strain with paragneiss (Fig. 7 and 8). A constrictional strain regime characterised by ubiquitous stretching lineations (L2) and L>S type tectonites is associated with S2a foliations in meta-igneous units. In contrast, a plane strain regime defined by S-L tectonites is supported by S2b foliations in the micas-rich paragneiss. S2a foliations are locally transposed by S2b foliations (Fig. 3), and microstructure analyses indicate higher deformation temperatures in ortho-derived units than in paragneiss (Fig. 10). These observations suggest a two-phases progressive deformation event during the retrograde metamorphic evolution associated with the collapse of the belt.

We propose a two-phase model in which two intermediate deformation phases represent increments of a progressive deformation during the evolution of a single transtensionnal event. The first phase involves the deformation at mid-crustal depth of all lithological units by a gently-dipping constrictional strain, creating L>S tectonites and the S2a foliation. This phase represents the sub-horizontal flow of the migmatitic crust at high temperatures. Some parts of the crust with a higher degree of anatexis are partially preserved from tectonic forces and experience doming and internal buoyancy-driven flow, as seen in the Super-Cannes hill (see section 5.2). The second phase is characterised by a plane strain flow that develops the S2b foliation and associated strike-slip shear zones. Deformation is partitioned into the paragneiss unit, enveloping ortho-derived lithologies that preserve their stretched shape from the first phase and are generally not or less overprinted. At the map scale, orthogneiss in the Reyran zone can be seen as finite strain markers representing prolate cigar-like bodies, shaped by the interaction of their internal stretching lineations direction and plunge with the topography. The plane strain deformation starts at high temperatures following the first phase, as observed in the western parts of the Cannes migmatites, but intensifies at lower temperatures in the paragneiss unit during the subsequent cooling of the hot crust. A strain gradient from the Cannes migmatites to the La Moure SZ is accompanied by a deformation-related temperature gradient from near solidus to chlorite isograd (Fig. 10). This indicates that during the second phase, deformation begins at high temperatures across the entire area before progressively localising westward at lower temperatures, following a strain softening until the onset of the La Moure SZ. The high strain SZ remains active until low temperatures leading to cataclastic flow and the opening of the Reyran pull-apart basin in which L-tectonite blocks are found within the conglomerates.

These two deformation phases highlight changes in the global transtensional regime, which could be represented by a combination of strike-slip and coaxial perpendicular extension (Fig. 11). During the first phase, the pure shear orthogonal component (prolate fabrics) dominates over the simple shear component. In contrast, the second phase is characterised by a simple shear-dominated flow represented by plane strain fabrics and vertical SZ. This progressive change of the transtensional regime could reflect an evolution of the transport direction. The switch from a first S2a foliation overprinted by the subsequent S2b foliation would represent a rotation of the extension direction becoming more parallel to the transcurrent shear direction. In fact, when the angle between the transport direction and the transtension zone boundary is greater than 20°, the coaxial component associated with vertical shortening and horizontal foliation dominate, while for angles less than 20° the transtension is dominated by the non-coaxial component, horizontal shortening and vertical foliation (Dewey, 2002; Teyssier and Tikoff, 1999). A second option is to consider the rheological influence on strain evolution due to cooling and preferential hydration of the crust during its progressive exhumation. In this hypothesis, the first constriction (pure shear) dominated transtension would be only possible with a hot crust which needs to be sufficiently weak to flow horizontally. Then, the progressive cooling and crystallisation of the crust will inhibit constrictional flow and promote strain localisation in the weaker paragneiss, leading to a simple shear dominated transtension.

Deformation localisation in the paragneiss unit during the second phase, rather than in meta-igneous rocks, exemplifies rheologically driven strain partitioning (Carreras et al., 2013; Fossen et al., 2019). After the crystallisation of anatectic melt, weak phases other than melt control the rheology of metamorphic rocks (Diener and Fagereng, 2014; Hunter et al., 2016; Vanardois, 2021). The Tanneron massif's progressive exhumation leads to the crystallisation of meta-igneous rocks, which gradually strengthen these units, acting as stronger homogenous bodies within the weaker heterogeneous paragneiss unit. The high rheologic contrast of meta-igneous rocks may deflect strain paths and localise them in surrounding weaker units (Gremmel et al., 2023). The paragneiss unit also contains a higher mica modal proportion than meta-igneous rocks, which is the weakest mineralogical phase and would control strain localisation at subsolidus conditions (Handy, 1994; Hunter et al., 2016; Montési, 2013). Typically, micaceous rocks deform more easily than quartzo-feldspathic rocks (Fossen et al., 2019). Strain localisation is also expected within rocks with layered fabrics (Handy, 1990; Hunter et al., 2016; Montési, 2013), especially with micaceous fabrics (Shea and Kronenberg, 1993; Wintsch et al., 1995), as seen in the meta-sediment unit compared to the meta-igneous units. This concept is sometimes referred to as "geometric softening" (Fossen and Cavalcante, 2017; Ji et al., 2004; Passchier and Trouw, 2005; Rutter et al., 2001). Consequently, the plane strain deformation phase in the study area progressively localises in the paragneiss unit during retrogression from sub-solidus down to low metamorphic grade due to strain hardening of crystallising meta-igneous units, creating a strong rheologic and geometric contrast. This strain partitioning arises during a general transtensive regime associated with the progressive oblique thinning of this collapsing hot orogen.

6. Conclusion

The preserved migmatitic basement of the eastern Tanneron massif lies in a crucial position between coeval deformation of partially molten rocks and opening of a pull apart basin, providing a unique opportunity to study the progressive collapse of a hot orogen during an oblique tectonic event. The study of this late Variscan oblique regime reveals a main transtensional kinematic divided in two intermediate deformation phases. The first phase depicts a subhorizontal flow with dominant constrictional fabrics (L>S tectonites) and minor gently dipping foliations at high temperature conditions. Then, a simple shear flow characterised by plane strain fabrics (S-L tectonites) with vertical foliations and subhorizontal lineations was active from high to low temperature conditions. Vertical foliations are distributed in a widespread network of anastomosed shear zones with a main dextral kinematic represented by the major La Moure SZ which was active until the opening of the Reyran carboniferous basin. The transition between the two phases is not interrupted, deformation was progressive in the same general transtensional regime and the two phases may have been synchronous for a while.

The field-based model presented in this study highlights important aspects of 3D strain distribution in ductile oblique regime and can contribute to better understanding these complex structural frameworks and related strain patterns. These findings will be useful as a template to compare with other suspected transtensional systems in hot orogen, and particularly with the numerous Variscan massifs described by late oblique deformation synchronously to the opening of Carboniferous basins. In addition, the progressive strain evolution from suprasolidus deformation down to greenschist facies until brittle deformation with the opening of a pull apart basin show how transtensional regime could efficiently and quickly lead to the exhumation of an unstable thicken crust.

The present study further illustrates how multi-method structural analysis, here through precise digital mapping coupled with complementary microstructural observations and finite strain quantification, are necessary to unravel and classify different strain patterns and their evolution in complex structural domains such as oblique tectonic.

Declaration of competing interest

The authors declare that there are no competing financial interests and neither personal relationships that could have appeared to influence the work reported in this paper.

Copyright

Acknowledgements

Jean-Marc Lardeaux and Pierre Trap are gratefully acknowledged for stimulating discussions. We also thank Pierre Trap for his generous support of a Keyence microscope providing high-resolution microphotography. This work was supported by the Tellus Program of CNRS-INSU, the CSI program of Université Côte d'Azur, and Géoazur Laboratory.

References

Alvarado, D., DeMets, C., Tikoff, B., Hernández, D., Wawrzyniec, T. F., Pullinger, C., Mattioli, G., Turner, H. L., Rodriguez, M., & Correa-Mora, F. (2011). Forearc motion and deformation between El Salvador and Nicaragua: GPS, seismic, structural, and paleomagnetic observations. *Lithosphere*, *3*(1), 3–21. https://doi.org/10.1130/L108.1

Archanjo, C. J., Trindade, R. I. F., Bouchez, J. L., & Ernesto, M. (2002). Granite fabrics and regional-scale strain partitioning in the Seridó belt (Borborema Province, NE Brazil). *Tectonics*, *21*(1), 3-1-3–14. https://doi.org/10.1029/2000TC001269

Asti, R., Saspiturry, N., & Angrand, P. (2022). The Mesozoic Iberia-Eurasia diffuse plate boundary: A wide domain of distributed transtensional deformation progressively focusing along the North Pyrenean Zone. *Earth-Science Reviews*, *230*, 104040. https://doi.org/10.1016/j.earscirev.2022.104040

Autin, J., Bellahsen, N., Husson, L., Beslier, M.-O., Leroy, S., & d'Acremont, E. (2010). Analog models of oblique rifting in a cold lithosphere. *Tectonics*, *29*(6). https://doi.org/10.1029/2010TC002671

Bascou, J., Henry, B., Ménot, R.-P., Funaki, M., & Barruol, G. (2013). Contribution of AMS measurements in understanding the migmatitic terrains of Pointe Géologie, Terre Adélie (East-Antarctica). *Tectonophysics*, *603*, 123–135. https://doi.org/10.1016/j.tecto.2013.05.021

Bellot, J.-P. (2005). The Palaeozoic evolution of the Maures massif (France) and its potential correlation with others areas of the Variscan belt: A review. *Journal of The Virtual Explorer*, *19*. https://doi.org/10.3809/jvirtex.2005.00116

Bolle, O., Corsini, M., Diot, H., Laurent, O., & Melis, R. (2023). Late-Orogenic Evolution of the Southern European Variscan Belt Constrained by Fabric Analysis and Dating of the Camarat Granitic Complex and Coeval Felsic Dykes (Maures–Tanneron Massif, SE France). *Tectonics*, *42*(4), e2022TC007310. https://doi.org/10.1029/2022TC007310

Borradaile, G. J., & Henry, B. (1997). Tectonic applications of magnetic susceptibility and its anisotropy. *Earth-Science Reviews*, *42*(1), 49–93. https://doi.org/10.1016/S0012-8252(96)00044-X

Borradaile, G. J., & Jackson, M. (2010). Structural geology, petrofabrics and magnetic fabrics (AMS, AARM, AIRM). *Journal of Structural Geology*, *32*(10), 1519–1551. https://doi.org/10.1016/j.jsg.2009.09.006

Bouchez, J.-L. (2000). Magnetic susceptibility anisotropy and fabrics in granites. *Comptes Rendus de l'Academie des Sciences Series IIA Earth and Planetary Science*, *1*(330), 1–14.

Brune, S. (2014). Evolution of stress and fault patterns in oblique rift systems: 3-D numerical lithospheric-scale experiments from rift to breakup. *Geochemistry, Geophysics, Geosystems*, *15*(8), 3392–3415. https://doi.org/10.1002/2014GC005446

Buscail, F. (2000). *Contribution à la compréhension du problème géologique et géodynamique du massif des maures: Le Métamorphisme régional modélisé dans le système KFMASH : analyse pargénétique, chémiographie, thermobarométrie, géochronologie Ar / Ar*.

Carosi, R., Montomoli, C., Tiepolo, M., & Frassi, C. (2012). Geochronological constraints on post-collisional shear zones in the Variscides of Sardinia (Italy). *Terra Nova*, *24*(1), 42–51. https://doi.org/10.1111/j.1365-3121.2011.01035.x

Carreras, J., Cosgrove, J. W., & Druguet, E. (2013). Strain partitioning in banded and/or anisotropic rocks: Implications for inferring tectonic regimes. *Journal of Structural Geology*, *50*, 7–21. https://doi.org/10.1016/j.jsg.2012.12.003

Cashman, S. M., Kelsey, H. M., Erdman, C. F., Cutten, H. N. C., & Berryman, K. R. (1992). Strain Partitioning between structural domains in the forearc of the Hikurangi

Subduction Zone, New Zealand. *Tectonics*, *11*(2), 242–257. https://doi.org/10.1029/91TC02363

Chardon, D., Aretz, M., & Roques, D. (2020). Reappraisal of Variscan tectonics in the southern French Massif Central. *Tectonophysics*, *787*, 228477. https://doi.org/10.1016/j.tecto.2020.228477

Chardon, D., Gapais, D., & Cagnard, F. (2009). Flow of ultra-hot orogens: A view from the Precambrian, clues for the Phanerozoic. *Tectonophysics*, *477*(3), 105–118. https://doi.org/10.1016/j.tecto.2009.03.008

Chardon, D., Jayananda, M., & Peucat, J.-J. (2011). Lateral constrictional flow of hot orogenic crust: Insights from the Neoarchean of south India, geological and geophysical implications for orogenic plateaux. *Geochemistry, Geophysics, Geosystems*, *12*(2). https://doi.org/10.1029/2010GC003398

Chorowicz, J., & Sorlien, C. (1992). Oblique extensional tectonics in the Malawi Rift, Africa. *Geological Society of America Bulletin - GEOL SOC AMER BULL*, *104*, 1015–1023. https://doi.org/10.1130/0016-7606(1992)104<1015:OETITM>2.3.CO;2

Clegg, P., & Holdsworth, R. E. (2005). Complex deformation as a result of strain partitioning in transpression zones: An example from the Leinster Terrane, SE Ireland. *Journal of the Geological Society*, *162*(1), 187–202. https://doi.org/10.1144/0016-764903-177

Corsini, M., Bosse, V., Féraud, G., Demoux, A., & Crevola, G. (2010). Exhumation processes during post-collisional stage in the Variscan belt revealed by detailed

40Ar/39Ar study (Tanneron Massif, SE France). *International Journal of Earth Sciences*, *99*(2), 327–341. https://doi.org/10.1007/s00531-008-0397-x

Corsini, M., & Rolland, Y. (2009). Late evolution of the southern European Variscan belt: Exhumation of the lower crust in a context of oblique convergence. *Comptes Rendus Geoscience*, *341*(2–3), 214–223. https://doi.org/10.1016/j.crte.2008.12.002

Crevola, G. (1977). *Etude petrographique et structurale de la partie orientale du massif de Tanneron (Provence cristalline).*

Cruden, A. R. (1988). Deformation around a rising diapir modeled by creeping flow past a sphere. *Tectonics*, *7*(5), 1091–1101. https://doi.org/10.1029/TC007i005p01091

Cruden, A. R. (1990). Flow and Fabric Development during the Diapiric Rise of Magma. *The Journal of Geology*, *98*(5), 681–698. https://doi.org/10.1086/629433

DARROZES, J., MOISY, M., OLIVIER, P., AMEGLIO, L., & BOUCHEZ, J.-L. (1994). Structure magmatique du granite du Sidobre (Tarn, France): De l'échelle du massif à celle de l'échantillon. *Structure Magmatique Du Granite Du Sidobre (Tarn, France) : De l'échelle Du Massif à Celle de l'échantillon*, *318*(2), 243–250.

Das, J. P., Bhattacharyya, K., & Mamtani, M. A. (2021). A kinematic approach for investigating magnetic and strain fabrics from constrictional and flattening domains of shear zones in Sikkim Himalayan fold thrust belt. *Journal of Structural Geology*, *149*, 104388. https://doi.org/10.1016/j.jsg.2021.104388

De Paola, N., Holdsworth, R. E., McCaffrey, K. J. W., & Barchi, M. R. (2005). Partitioned transtension: An alternative to basin inversion models. *Journal of Structural Geology*, *27*(4), 607–625. https://doi.org/10.1016/j.jsg.2005.01.006

Demoux, A., SCHäRER, U., & CORSINI, M. (2008). Variscan evolution of the Tanneron massif, SE France, examined through U–Pb monazite ages. *Journal of the Geological Society*, *165*(2), 467–478. https://doi.org/10.1144/0016-76492007-045

Denèle, Y., Roques, D., Ganne, J., Chardon, D., Rousse, S., & Barbey, P. (2017). Strike-slip metamorphic core complexes: Gneiss domes emplaced in releasing bends. *Geology*, *45*(10), 903–906. https://doi.org/10.1130/G39065.1

Dewey, J. F. (2002). Transtension in Arcs and Orogens. *International Geology Review*, *44*(5), 402–439. https://doi.org/10.2747/0020-6814.44.5.402

Dewey, J. F., Holdsworth, R. E., & Strachan, R. A. (1998). Transpression and transtension zones. *Geological Society, London, Special Publications*, *135*(1), 1–14. https://doi.org/10.1144/GSL.SP.1998.135.01.01

Diener, J. F. A., & Fagereng, Å. (2014). The influence of melting and melt drainage on crustal rheology during orogenesis. *Journal of Geophysical Research: Solid Earth*, *119*(8), 6193–6210. https://doi.org/10.1002/2014JB011088

Dirks, P. H. G. M., Zhang, J. S., & Passchier, C. W. (1997). Exhumation of high-pressure granulites and the role of lower crustal advection in the North China Craton near Datong. *Journal of Structural Geology*, *19*(10), 1343–1358. https://doi.org/10.1016/S0191-8141(97)00044-8

Dixon, J. M. (1975). Finite strain and progressive deformation in models of diapiric structures. *Tectonophysics*, *28*(1), 89–124. https://doi.org/10.1016/0040-1951(75)90060-8

Djouadi, M. T., Gleizes, G., Ferré, E., Bouchez, J. L., Caby, R., & Lesquer, A. (1997). Oblique magmatic structures of two epizonal granite plutons, Hoggar, Algeria: Late-orogenic emplacement in a transcurrent orogen. *Tectonophysics*, *279*(1), 351–374. https://doi.org/10.1016/S0040-1951(97)00123-6

Duchesne, J.-C., Liégeois, J.-P., Bolle, O., Vander Auwera, J., Bruguier, O., Matukov, D. I., & Sergeev, S. A. (2013). The fast evolution of a crustal hot zone at the end of a transpressional regime: The Saint-Tropez peninsula granites and related dykes (Maures Massif, SE France). *Lithos*, *162–163*, 195–220. https://doi.org/10.1016/j.lithos.2012.12.019

Duclaux, G., Huismans, R. S., & May, D. A. (2020). Rotation, narrowing, and preferential reactivation of brittle structures during oblique rifting. *Earth and Planetary Science Letters*, *531*, 115952. https://doi.org/10.1016/j.epsl.2019.115952

Ebert, A., Herwegh, M., & Pfiffner, A. (2007). Cooling induced strain localization in carbonate mylonites within a large-scale shear zone (Glarus thrust, Switzerland). *Journal of Structural Geology*, *29*(7), 1164–1184. https://doi.org/10.1016/j.jsg.2007.03.007

Edel, J. B., Schulmann, K., Lexa, O., & Lardeaux, J. M. (2018). Late Palaeozoic palaeomagnetic and tectonic constraints for amalgamation of Pangea supercontinent in the European Variscan belt. *Earth-Science Reviews*, *177*, 589–612. https://doi.org/10.1016/j.earscirev.2017.12.007

Faleiros, F. M., Ribeiro, B. V., Campanha, G. A. C., Cawood, P. A., Cabrita, D. I. G., Yogi, M. T. A. G., Milani, L. A., Lemos-Santos, D. V., Almeida, V. V., Rodrigues, S. W. O., Malta, I. S., & Forero-Ortega, A. J. (2022). Strain Partitioning along Terrane Bounding and Intraterrane Shear Zones: Constraints from a Long-Lived Transpressional System in West Gondwana (Ribeira Belt, Brazil). *Lithosphere*, *2021*(Special 6), 2103213. https://doi.org/10.2113/2022/2103213

Ferranti, L., Santoro, E., Mazzella, M. E., Monaco, C., & Morelli, D. (2009). Active transpression in the northern Calabria Apennines, southern Italy. *Tectonophysics*, *476*(1–2), 226–251. https://doi.org/10.1016/j.tecto.2008.11.010

Fletcher, J. M., & Bartley, J. M. (1994). Constrictional strain in a non-coaxial shear zone: Implications for fold and rock fabric development, central mojave metamorphic core complex, california. *Journal of Structural Geology*, *16*(4), 555–570. https://doi.org/10.1016/0191-8141(94)90097-3

Fossen, H. (2016). *Structural Geology*. Cambridge University Press.

Fossen, H., & Cavalcante, G. C. G. (2017). Shear zones – A review. *Earth-Science Reviews*, *171*, 434–455. https://doi.org/10.1016/j.earscirev.2017.05.002

Fossen, H., Cavalcante, G. C. G., Pinheiro, R. V. L., & Archanjo, C. J. (2019). Deformation – Progressive or multiphase? *Journal of Structural Geology*, *125*, 82–99. https://doi.org/10.1016/j.jsg.2018.05.006

Fossen, H., Teyssier, C., & Whitney, D. L. (2013). Transtensional folding. *Journal of Structural Geology*, *56*, 89–102. https://doi.org/10.1016/j.jsg.2013.09.004

Fossen, H., & Tikoff, B. (1993). The deformation matrix for simultaneous simple shearing, pure shearing and volume change, and its application to transpression-transtension tectonics. *Journal of Structural Geology*, *15*(3), 413–422. https://doi.org/10.1016/0191-8141(93)90137-Y

Fossen, H., & Tikoff, B. (1998). Extended models of transpression and transtension, and application to tectonic settings. *Geological Society, London, Special Publications*, *135*(1), 15–33. https://doi.org/10.1144/GSL.SP.1998.135.01.02

Fossen, H., Tikoff, B., & Teyssier, C. (1994). Strain modeling of transpressional and transtensional deformation. *Norsk Geologisk Tidsskrift*, *74*(3), 134–145.

Franke, W., Doublier, M. P., Klama, K., Potel, S., & Wemmer, K. (2011). Hot metamorphic core complex in a cold foreland. *International Journal of Earth Sciences*, *100*(4), 753–785. https://doi.org/10.1007/s00531-010-0512-7

Frassi, C., Carosi, R., Montomoli, C., & Law, R. D. (2009). Kinematics and vorticity of flow associated with post-collisional oblique transpression in the Variscan Inner Zone of northern Sardinia (Italy). *Journal of Structural Geology*, *31*(12), 1458–1471. https://doi.org/10.1016/j.jsg.2009.10.001

Gapais, D. (1989). Shear structures within deformed granites: Mechanical and thermal indicators. *Geology*, *17*(12), 1144–1147. https://doi.org/10.1130/0091-7613(1989)017<1144:SSWDGM>2.3.CO;2

Gapais, D., Pelletier, A., Ménot, R.-P., & Peucat, J.-J. (2008). Paleoproterozoic tectonics in the Terre Adélie Craton (East Antarctica). *Precambrian Research*, *162*(3), 531–539. https://doi.org/10.1016/j.precamres.2007.10.011

Gapais, D., Potrel, A., Machado, N., & Hallot, E. (2005). Kinematics of long-lasting Paleoproterozoic transpression within the Thompson Nickel Belt, Manitoba, Canada. *Tectonics*, *24*(3). https://doi.org/10.1029/2004TC001700

Gattacceca, J. (2000). *Cinématique du bassin liguro-provençal entre 30 et 12 Ma. Implication géodynamiques* [These de doctorat, Paris, ENMP]. https://www.theses.fr/2000ENMP1060

Gébelin, A., Brunel, M., Monié, P., Faure, M., & Arnaud, N. (2007). Transpressional tectonics and Carboniferous magmatism in the Limousin, Massif Central, France: Structural and 40Ar/39Ar investigations. *Tectonics*, *26*(2). https://doi.org/10.1029/2005TC001822

Gerbault, M., Schneider, J., Reverso-Peila, A., & Corsini, M. (2018). Crustal exhumation during ongoing compression in the Variscan Maures-Tanneron Massif, France-Geological and thermo-mechanical aspects. *Tectonophysics*, *746*, 439–458. https://doi.org/10.1016/j.tecto.2016.12.019

Ghosh, S. K., Khan, D., & Sengupta, S. (1995). Interfering folds in constrictional deformation. *Journal of Structural Geology*, *17*(10), 1361–1373. https://doi.org/10.1016/0191-8141(95)00027-B

Giacomini, F., Dallai, L., Carminati, E., Tiepolo, M., & Ghezzo, C. (2008). Exhumation of a Variscan orogenic complex: Insights into the composite granulitic–amphibolitic metamorphic basement of south-east Corsica (France). *Journal of Metamorphic Geology*, *26*(4), 403–436. https://doi.org/10.1111/j.1525-1314.2008.00768.x

Goodwin, L. B., & Tikoff, B. (2002). Competency contrast, kinematics, and the development of foliations and lineations in the crust. *Journal of Structural Geology*, *24*(6), 1065–1085. https://doi.org/10.1016/S0191-8141(01)00092-X

Goodwin, L. B., & Williams, P. F. (1996). Deformation path partitioning within a transpressive shear zone, Marble Cove, Newfoundland. *Journal of Structural Geology*, *18*(8), 975–990. https://doi.org/10.1016/0191-8141(96)00015-6

Gremmel, J., Trap, P., Le Bayon, B., Mumba, R., Fullgraf, T., & Lach, P. (2023). Tectono-metamorphic evolution and strain partitioning along the Mugesse mega shear zone, Ubendian Belt (Northern Malawi). *Journal of African Earth Sciences*, *205*, 104949. https://doi.org/10.1016/j.jafrearsci.2023.104949

Handy, M. R. (1990). The solid-state flow of polymineralic rocks. *Journal of Geophysical Research: Solid Earth*, *95*(B6), 8647–8661. https://doi.org/10.1029/JB095iB06p08647

Handy, M. R. (1994). Flow laws for rocks containing two non-linear viscous phases: A phenomenological approach. *Journal of Structural Geology*, *16*(3), 287–301. https://doi.org/10.1016/0191-8141(94)90035-3

Harland, W. B. (1971). Tectonic transpression in Caledonian Spitsbergen. *Geological Magazine*, *108*(1), 27–41. https://doi.org/10.1017/S0016756800050937

Henry, B., Merabet, N., Derder, M. E. M., & Bayou, B. (2004). Chemical remagnetizations in the Illizi basin (Saharan craton, Algeria) and their acquisition process. *Geophysical Journal International*, *156*(2), 200–212. https://doi.org/10.1111/j.1365-246X.2003.02106.x

Hrouda, F. (2002). The use of the anisotropy of magnetic remanence in the resolution of the anisotropy of magnetic susceptibility into its ferromagnetic and paramagnetic components. *Tectonophysics*, *347*(4), 269–281. https://doi.org/10.1016/S0040-1951(02)00075-6

Hunter, N. J. R., Hasalová, P., Weinberg, R. F., & Wilson, C. J. L. (2016). Fabric controls on strain accommodation in naturally deformed mylonites: The influence of interconnected micaceous layers. *Journal of Structural Geology*, *83*, 180–193. https://doi.org/10.1016/j.jsg.2015.12.005

Jackson, M. (1991). Anisotropy of magnetic remanence: A brief review of mineralogical sources, physical origins, and geological applications, and comparison with susceptibility anisotropy. *Pure and Applied Geophysics*, *136*(1), 1–28. https://doi.org/10.1007/BF00878885

Jelínek, V. (1978). Statistical processing of anisotropy of magnetic susceptibility measured on groups of specimens. *Studia Geophysica et Geodaetica*, *22*(1), 50–62. https://doi.org/10.1007/BF01613632

Jelinek, V. (1981). Characterization of the magnetic fabric of rocks. *Tectonophysics*, *79*(3), T63–T67. https://doi.org/10.1016/0040-1951(81)90110-4

Ji, S., Jiang, Z., Rybacki, E., Wirth, R., Prior, D., & Xia, B. (2004). Strain softening and microstructural evolution of anorthite aggregates and quartz–anorthite layered composites deformed in torsion. *Earth and Planetary Science Letters*, *222*(2), 377–390. https://doi.org/10.1016/j.epsl.2004.03.021

Jiang, D. (1994a). Flow variation in layered rocks subjected to bulk flow of various kinematic vorticities: Theory and geological implications. *Journal of Structural Geology*, *16*(8), 1159–1172. https://doi.org/10.1016/0191-8141(94)90059-0

Jiang, D. (1994b). Vorticity determination, distribution, partitioning and the heterogeneity and non-steadiness of natural deformations. *Journal of Structural Geology*, *16*(1), 121–130. https://doi.org/10.1016/0191-8141(94)90023-X

Jones, R. R., Holdsworth, R. E., Clegg, P., McCaffrey, K., & Tavarnelli, E. (2004). Inclined transpression. *Journal of Structural Geology*, *26*(8), 1531–1548. https://doi.org/10.1016/j.jsg.2004.01.004

Klepeis, K. A., Schwartz, J. J., Miranda, E., Lindquist, P., Jongens, R., Turnbull, R., & Stowell, H. (2022). The Initiation and Growth of Transpressional Shear Zones Through Continental Arc Lithosphere, Southwest New Zealand. *Tectonics*, *41*(9), e2021TC007097. https://doi.org/10.1029/2021TC007097

Kruckenberg, S. C., Vanderhaeghe, O., Ferré, E. C., Teyssier, C., & Whitney, D. L. (2011). Flow of partially molten crust and the internal dynamics of a migmatite dome, Naxos, Greece. *Tectonics*, *30*(3). https://doi.org/10.1029/2010TC002751

Le Pourhiet, L., Huet, B., May, D. A., Labrousse, L., & Jolivet, L. (2012). Kinematic interpretation of the 3D shapes of metamorphic core complexes. *Geochemistry, Geophysics, Geosystems*, *13*(9). https://doi.org/10.1029/2012GC004271

Lee, A. L., Torvela, T., Lloyd, G. E., & Walker, A. M. (2018). Melt organisation and strain partitioning in the lower crust. *Journal of Structural Geology*, *113*, 188–199. https://doi.org/10.1016/j.jsg.2018.05.016

Lister, G. S., & Williams, P. F. (1983). The partitioning of deformation in flowing rock masses. *Tectonophysics*, *92*(1), 1–33. https://doi.org/10.1016/0040-1951(83)90083-5

Maillet, A. (2021). *Cartographie et analyse structurale du bassin Carbonifère du Reyran, massif de Tanneron (Maures-Tanneron)*. https://doi.org/10.13140/RG.2.2.22163.25122/1

Meghraoui, M., & Pondrelli, S. (2012). Active faulting and transpression tectonics along the plate boundary in North Africa. *Annals of Geophysics*, *55*(5), 955–967. https://doi.org/10.4401/ag-4970

Monnier, O. (1995). *Le socle protérozoique de terre Adélie (Antarctique est): Son évolution tectono-métamorphique et sa place dans les reconstitutions du proto-gondwana* [These de doctorat, Saint-Etienne]. https://www.theses.fr/1995STET4018

Montési, L. G. J. (2013). Fabric development as the key for forming ductile shear zones and enabling plate tectonics. *Journal of Structural Geology*, *50*, 254–266. https://doi.org/10.1016/j.jsg.2012.12.011

Morley, C. K., Haranya, C., Phoosongsee, W., Pongwapee, S., Kornsawan, A., & Wonganan, N. (2004). Activation of rift oblique and rift parallel pre-existing fabrics during extension and their effect on deformation style: Examples from the rifts of Thailand. *Journal of Structural Geology*, *26*(10), 1803–1829. https://doi.org/10.1016/j.jsg.2004.02.014

Mount, V. S., & Suppe, J. (1992). Present-day stress orientations adjacent to active strike-slip faults: California and Sumatra. *Journal of Geophysical Research: Solid Earth*, *97*(B8), 11995–12013. https://doi.org/10.1029/92JB00130

Nédélec, A., & Bouchez, J.-L. (2015). *Granites: Petrology, Structure, Geological Setting, and Metallogeny*. OUP Oxford.

Norris, R. J., Koons, P. O., & Cooper, A. F. (1990). The obliquely-convergent plate boundary in the South Island of New Zealand: Implications for ancient collision zones. *Journal of Structural Geology*, *12*(5), 715–725. https://doi.org/10.1016/0191-8141(90)90084-C

Oldow, J. S., Bally, A. W., & Avé Lallemant, H. G. (1990). Transpression, orogenic float, and lithospheric balance. *Geology*, *18*(10), 991–994. https://doi.org/10.1130/0091-7613(1990)018<0991:TOFALB>2.3.CO;2

Oliot, E., Melleton, J., Schneider, J., Corsini, M., Gardien, V., & Rolland, Y. (2015). Variscan crustal thickening in the Maures-Tanneron massif (South Variscan belt, France): New in situ monazite U-Th-Pb chemical dating of high-grade rocks. *Bulletin de La*

Société Géologique de France, *186*(2–3), 145–169. https://doi.org/10.2113/gssgfbull.186.2-3.145

Onézime, J., Faure, M., & Crévola, G. (1999). Étude pétro-structurale du complexe granitique Rouet—Plan-de-la-Tour (massifs des Maures et du Tanneron occidental, Var). *Comptes Rendus de l'Académie des Sciences - Series IIA - Earth and Planetary Science*, *328*(11), 773–779. https://doi.org/10.1016/S1251-8050(99)80170-0

Orsini, J.-B. (1968). *Etude pétrographique et structurale du Massif du Tanneron (Var)—Parties occidentale et centrale* [PhD Thesis, Université de Grenoble]. https://theses.hal.science/tel-00688588

Passchier, C. W., & Trouw, R. A. J. (2005). *Microtectonics*. Springer Science & Business Media.

Paulsen, T. S., EncarnaciÓn, J., & Grunow, A. M. (2004). Structure and timing of transpressional deformation in the Shackleton Glacier area, Ross orogen, Antarctica. *Journal of the Geological Society*, *161*(6), 1027–1038. https://doi.org/10.1144/0016-764903-040

Pelletier, A. (2001). *Etude structurale et métamorphique du socle de Terre Adélie-George V Land (Est Antarctique): Un exemple de la transition Archéen/Paléoprotérozoïque* [These de doctorat, Saint-Etienne]. https://www.theses.fr/2001STET4015

Rey, P. F., Mondy, L., Duclaux, G., Teyssier, C., Whitney, D. L., Bocher, M., & Prigent, C. (2017). The origin of contractional structures in extensional gneiss domes. *Geology*, *45*(3), 263–266. https://doi.org/10.1130/G38595.1

Richard, P. D., Naylor, M. A., & Koopman, A. (1995). Experimental models of strike-slip tectonics. *Petroleum Geoscience*, *1*(1), 71–80. https://doi.org/10.1144/petgeo.1.1.71

Roberts, N. M., & Tikoff, B. (2021). Internal structure of the Paleoarchean Mt Edgar dome, Pilbara Craton, Western Australia. *Precambrian Research*, *358*, 106163. https://doi.org/10.1016/j.precamres.2021.106163

Rochette, P. (1987). Magnetic susceptibility of the rock matrix related to magnetic fabric studies. *Journal of Structural Geology*, *9*(8), 1015–1020. https://doi.org/10.1016/0191-8141(87)90009-5

Rochette, P., Jackson, M., & Aubourg, C. (1992). Rock magnetism and the interpretation of anisotropy of magnetic susceptibility. *Reviews of Geophysics*, *30*(3), 209–226. https://doi.org/10.1029/92RG00733

Rolland, Y., Corsini, M., & Demoux, A. (2009). Metamorphic and structural evolution of the Maures-Tanneron massif (SE Variscan chain): Evidence of doming along a transpressional margin. *Bulletin de La Société Géologique de France*, *180*(3), 217–230. https://doi.org/10.2113/gssgfbull.180.3.217

Rutter, E. H., Holdsworth, R. E., & Knipe, R. J. (2001). The nature and tectonic significance of fault-zone weakening: An introduction. *Geological Society, London, Special Publications*, *186*(1), 1–11. https://doi.org/10.1144/GSL.SP.2001.186.01.01

Sanderson, D. J., & Marchini, W. R. D. (1984). Transpression. *Journal of Structural Geology*, *6*(5), 449–458. https://doi.org/10.1016/0191-8141(84)90058-0

Schneider, J., Corsini, M., Reverso-Peila, A., & Lardeaux, J.-M. (2014). Thermal and mechanical evolution of an orogenic wedge during Variscan collision: An example in the Maures–Tanneron Massif (SE France). *Geological Society, London, Special Publications*, *405*(1), 313–331. https://doi.org/10.1144/SP405.4

Schreurs, G., & Colletta, B. (1998). Analogue modelling of faulting in zones of continental transpression and transtension. *Geological Society, London, Special Publications*, *135*(1), 59–79. https://doi.org/10.1144/GSL.SP.1998.135.01.05

Shan, Y. (2008). An analytical approach for determining strain ellipsoids from measurements on planar surfaces. *Journal of Structural Geology*, *30*(4), 539–546. https://doi.org/10.1016/j.jsg.2006.12.004

Shea, W. T., & Kronenberg, A. K. (1993). Strength and anisotropy of foliated rocks with varied mica contents. *Journal of Structural Geology*, *15*(9), 1097–1121. https://doi.org/10.1016/0191-8141(93)90158-7

Simonetti, M., Carosi, R., Montomoli, C., Corsini, M., Petroccia, A., Cottle, J. M., & Iaccarino, S. (2020). Timing and kinematics of flow in a transpressive dextral shear zone, Maures Massif (Southern France). *International Journal of Earth Sciences*, *109*(7), 2261–2285. https://doi.org/10.1007/s00531-020-01898-6

Skyttä, P., Hermansson, T., Elming, S.-Å., & Bauer, T. (2010). Magnetic fabrics as constraints on the kinematic history of a pre-tectonic granitoid intrusion, Kristineberg, northern Sweden. *Journal of Structural Geology*, *32*(8), 1125–1136. https://doi.org/10.1016/j.jsg.2010.06.020

Stipp, M., Stünitz, H., Heilbronner, R., & Schmid, S. M. (2002). Dynamic recrystallization of quartz: Correlation between natural and experimental conditions. *Geological Society, London, Special Publications*, *200*(1), 171–190. https://doi.org/10.1144/GSL.SP.2001.200.01.11

Stuart, C. A., Piazolo, S., & Daczko, N. R. (2018). The recognition of former melt flux through high-strain zones. *Journal of Metamorphic Geology*, *36*(8), 1049–1069. https://doi.org/10.1111/jmg.12427

Sullivan, W. A. (2006). Structural Significance of L Tectonites in the Eastern-Central Laramie Mountains, Wyoming. *The Journal of Geology*, *114*(5), 513–531. https://doi.org/10.1086/506158

Sullivan, W. A. (2008). Significance of transport-parallel strain variations in part of the Raft River shear zone, Raft River Mountains, Utah, USA. *Journal of Structural Geology*, *30*(2), 138–158. https://doi.org/10.1016/j.jsg.2007.11.007

Sullivan, W. A. (2013). L tectonites. *Journal of Structural Geology*, *50*, 161–175. https://doi.org/10.1016/j.jsg.2012.01.022

Sylvester, A. G., & Smith, R. R. (1976). Tectonic Transpression and Basement-Controlled Deformation in San Andreas Fault Zone, Salton Trough, California1. *AAPG Bulletin*, *60*(12), 2081–2102. https://doi.org/10.1306/C1EA3A73-16C9-11D7-8645000102C1865D

Talbot, C. J., & Jackson, M. P. A. (1987). Internal Kinematics of Salt Diapirs1. *AAPG Bulletin*, *71*(9), 1068–1093. https://doi.org/10.1306/703C7DF9-1707-11D7-8645000102C1865D

Teyssier, C., & Tikoff, B. (1998). Strike-slip partitioned transpression of the San Andreas fault system: A lithospheric-scale approach. *Geological Society, London, Special Publications*, *135*(1), 143–158. https://doi.org/10.1144/GSL.SP.1998.135.01.10

Teyssier, C., & Tikoff, B. (1999). Fabric stability in oblique convergence and divergence. *Journal of Structural Geology*, *21*(8), 969–974. https://doi.org/10.1016/S0191-8141(99)00067-X

Teyssier, C., Tikoff, B., & Markley, M. (1995). Oblique plate motion and continental tectonics. *Geology*, *23*. https://doi.org/10.1130/0091-7613(1995)023<0447:OPMACT>2.3.CO;2

Thevoux-Chabuel, H., MENOT, R.-P., LARDEAUX, J.-M., & MONNIER, O. (1995). Evolution tectono-métamorphique polyphasée paléozoïque dans le socle de Zicavo (Corse-du-Sud): Témoin d'un amincissement post-orogénique. *Evolution Tectono-Métamorphique Polyphasée Paléozoïque Dans Le Socle de Zicavo (Corse-Du-Sud): Témoin d'un Amincissement Post-Orogénique*, *321*(1), 47–56.

Tikoff, B., & Teyssier, C. (1994). Strain modeling of displacement-field partitioning in transpressional orogens. *Journal of Structural Geology*, *16*(11), 1575–1588. https://doi.org/10.1016/0191-8141(94)90034-5

Toutin-Morin, N., Crevola, G., Giraud, J. D., Dubar, M., Brocard, C., Dardeau, G., Bulard, P. F., Meinesz, A., & Bonijoly, D. (1994). *Carte géologique de la France à 1/50 000, feuille 1024 Fréjus-Cannes*. BRGM.

Umhoefer, P. J., & Dorsey, R. J. (1997). Translation of terranes: Lessons from central Baja California, Mexico. *Geology*, *25*(11), 1007–1010. https://doi.org/10.1130/0091-7613(1997)025<1007:TOTLFC>2.3.CO;2

Vanardois, J. (2021). *Fusion partielle, transfert de magma et partitionnement de la déformation au cours de l'orogénèse Varisque: Exemple des massifs des Aiguilles-Rouges (Alpes) et de l'Agly (Pyrénées)* [These de doctorat, Bourgogne Franche-Comté]. https://www.theses.fr/2021UBFCD067

Vauchez, P. A., & Bufalo, M. (1988). Charriage crustal, anatexie et decrochements ductiles dans les Maures orientales (Var, France) au cours de l'orogenese varisque. *Geologische Rundschau*, *77*(1), 45–62. https://doi.org/10.1007/BF01848675

Vollmer, F. W. (2018). Automatic contouring of geologic fabric and finite strain data on the unit hyperboloid. *Computers & Geosciences*, *115*, 134–142. https://doi.org/10.1016/j.cageo.2018.03.006

Wiest, J. D., Osmundsen, P. T., Jacobs, J., & Fossen, H. (2019). Deep Crustal Flow Within Postorogenic Metamorphic Core Complexes: Insights From the Southern Western Gneiss Region of Norway. *Tectonics*, *38*(12), 4267–4289. https://doi.org/10.1029/2019TC005708

Wilson, R. W., McCaffrey, K. J. W., Holdsworth, R. E., Imber, J., Jones, R. R., Welbon, A. I. F., & Roberts, D. (2006). Complex fault patterns, transtension and structural segmentation of the Lofoten Ridge, Norwegian margin: Using digital mapping to link onshore and offshore geology. *Tectonics*, *25*(4). https://doi.org/10.1029/2005TC001895

Wintsch, R. P., Christoffersen, R., & Kronenberg, A. K. (1995). Fluid-rock reaction weakening of fault zones. *Journal of Geophysical Research: Solid Earth*, *100*(B7), 13021–13032. https://doi.org/10.1029/94JB02622

Withjack, M. O., & Jamison, W. R. (1986). Deformation produced by oblique rifting. *Tectonophysics*, *126*(2), 99–124. https://doi.org/10.1016/0040-1951(86)90222-2

Zibra, I., Kruhl, J. H., Montanini, A., & Tribuzio, R. (2012). Shearing of magma along a high-grade shear zone: Evolution of microstructures during the transition from magmatic to solid-state flow. *Journal of Structural Geology*, *37*, 150–160. https://doi.org/10.1016/j.jsg.2012.01.011

FIGURE CAPTIONS

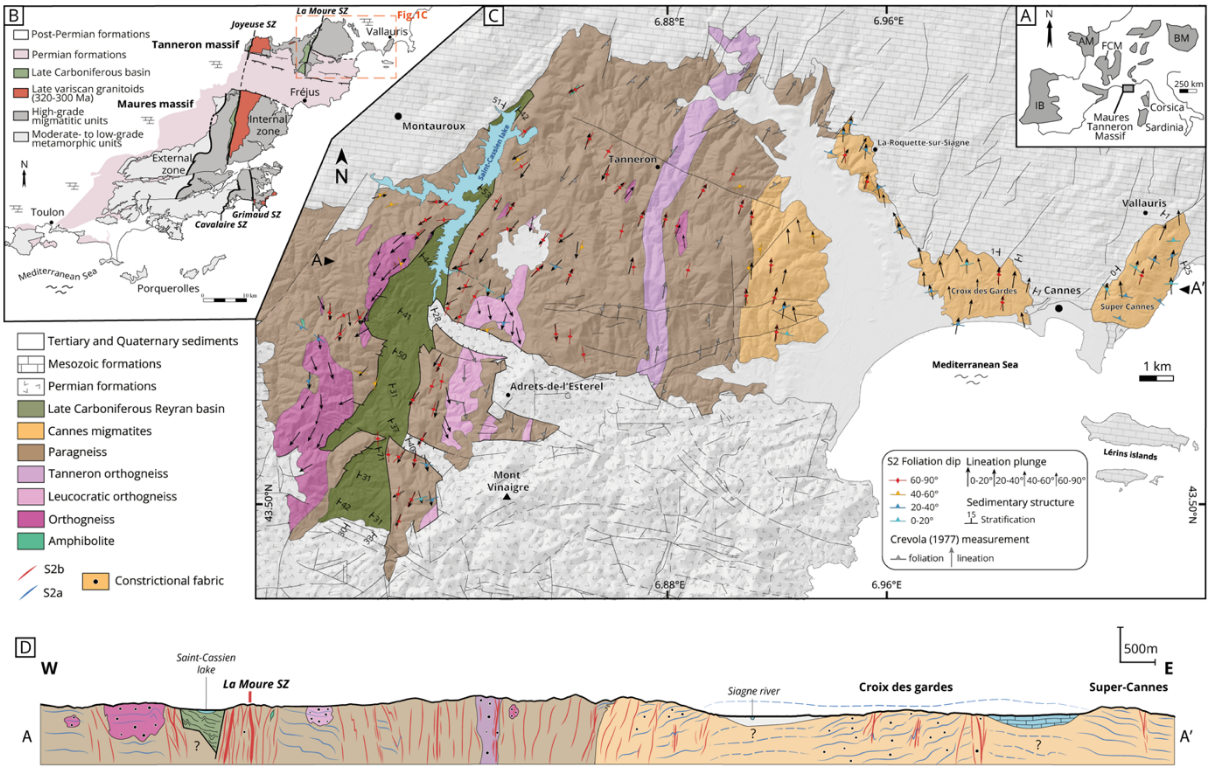

Figure 1: (A) Location of the Maures-Tanneron massif in western Europe with main Variscan massifs (IB: Iberian massif, AM: Armorican massif, FCM: French Central massif, BM: Bohemian massif) (modified from Gerbault et al., 2018). (B) Simplified tectonic map of the Maures-Tanneron massif. (C) Geological map of the eastern Tanneron. Location of the A-A' cross section below is indicated on the map. (D) Schematic cross section of the eastern Tanneron.

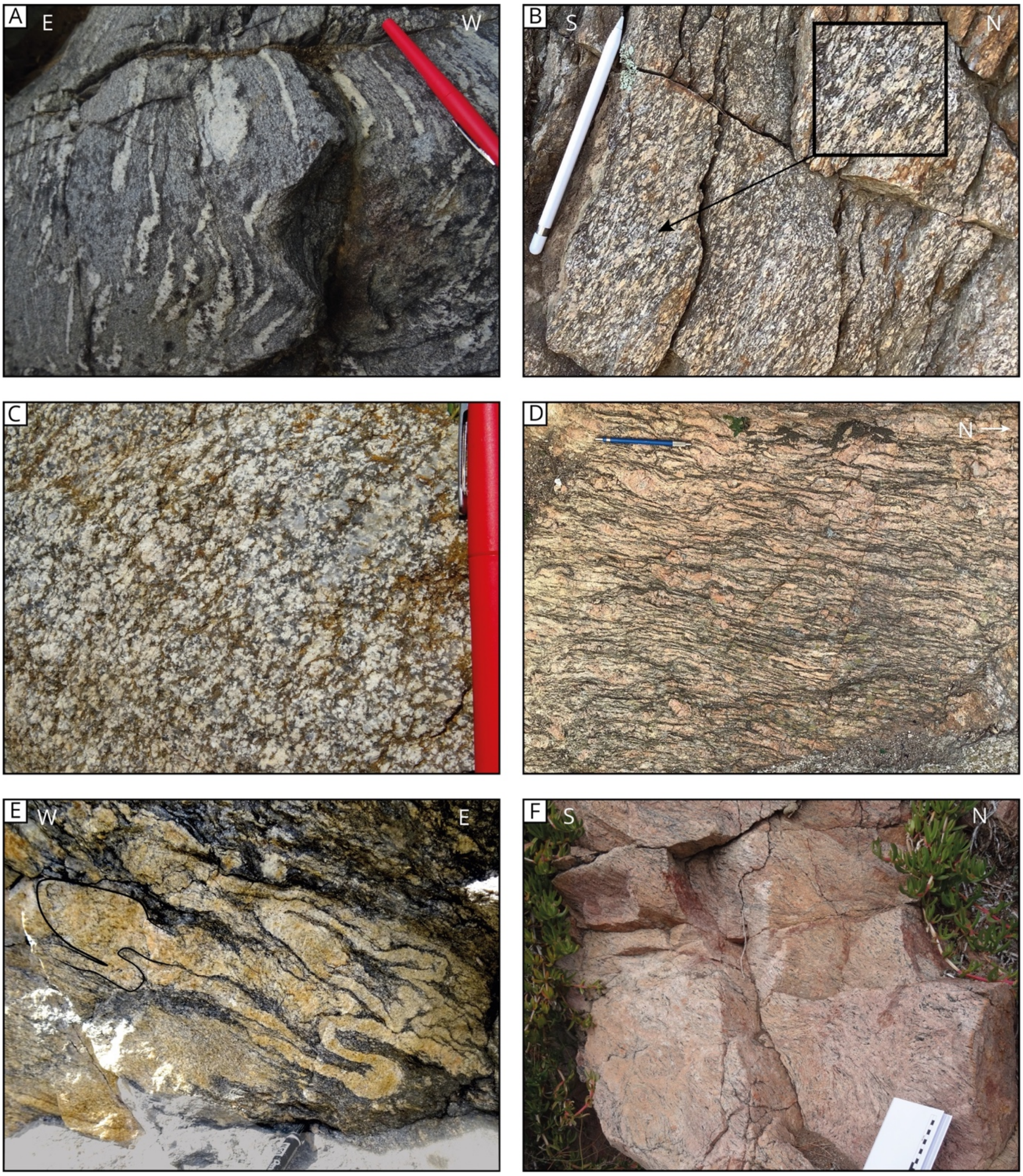

Figure 2: Photographs of the migmatitic paragneiss and orthogneiss and Cannes migmatites, showing their main lithological and structural appearance in the field. (A) The migmatitic paragneiss is a dark stromatic metapelite with visible regular centimetric leucosomes in low strain domain (GPS coordinates: 43.5711/6.8417). (B) The migmatitic orthogneiss commonly appears as a stretched micro-granite

with a homogenous texture of alternating lens or bands of leucocratic quartz-feldspar and dark biotite-muscovite (Sample JG21-02, 43.5301/6.7465). (C) Granitoid protolith of the migmatitic orthogneiss (B) visible in low strain local domain (43.5354/6.7620). (D) The Cannes migmatite is a stromatic migmatite, defined by pale pink to pale yellow thick irregular and coarse grain leucosomes alternating with thinner dark melanosomes. Centimetric augen K-feldspars are visible in the leucosome layers (43.5507/7.0108). (E) Migration of melt toward the hinge of similar folds in irregular leucosomes, indicative of high grade deformation synchronously to partial melting (Super-Cannes hill, 43.5732/7.0619). (F) Secondary facies of the Cannes migmatites with a higher degree of anatexis visible by the ubiquitous leucosomes over melanosomes, giving a nebulitic texture (43.5584/7.0645).

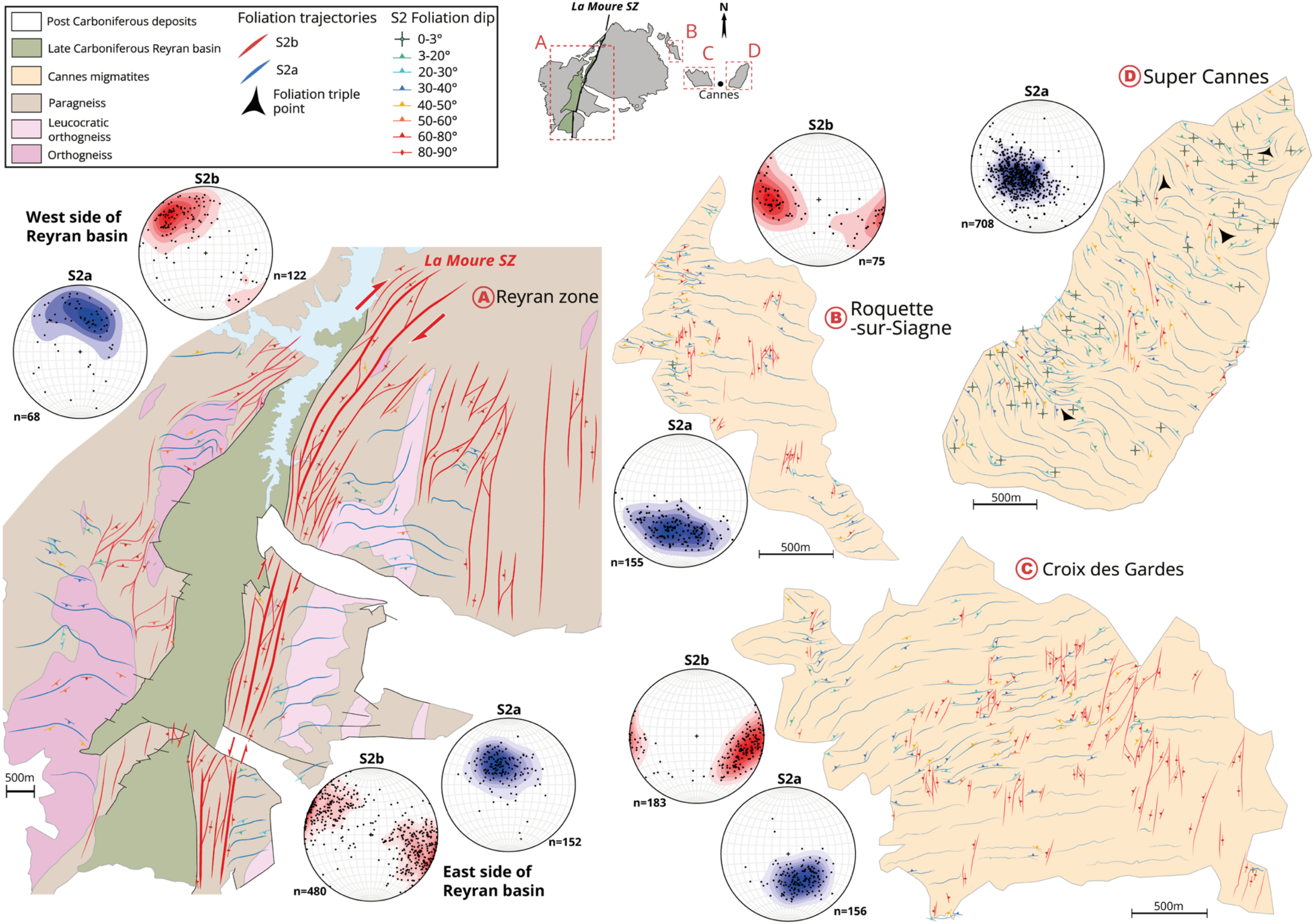
Post Carboniferous deposits
Late Carboniferous Reyran basin
Cannes migmatites
Paragneiss
Leucocratic orthogneiss
Orthogneiss
Foliation trajectories
S2b
S2a
Foliation triple point
S2 Foliation dip
0-3°
3-20°
20-30°
30-40°
40-50°
50-60°
60-80°
80-90°
La Moure SZ
A
B
C
D
N
Cannes
West side of Reyran basin
S2b
n=122
S2a
n=68
La Moure SZ
A Reyran zone
500m
S2b
n=480
S2a
n=152
East side of Reyran basin
S2b
n=75
B Roquette -sur-Siagne
S2a
n=155
500m
D Super Cannes
S2a
n=708
500m
C Croix des Gardes
S2b
n=183
S2a
n=156
500m

Figure 3: Structural maps showing foliation trajectories and highlighting the two strain patterns for the Reyran zone and the three Cannes hills. Lower hemisphere stereograms of foliation poles for the two planar fabric S2a and S2b are given close to their respective area. See the anastomosed network of the vertical La Moure SZ (S2b foliations) bounding the eastern side of the Reyran basin and which overprint S2a foliations as emphasised by the deflection of S2a foliation close to the SZ. The Super Cannes hill reveals highly variable S2a directions highlighted by the presence of foliation triple points and a concentric half-dome pattern in the western part.

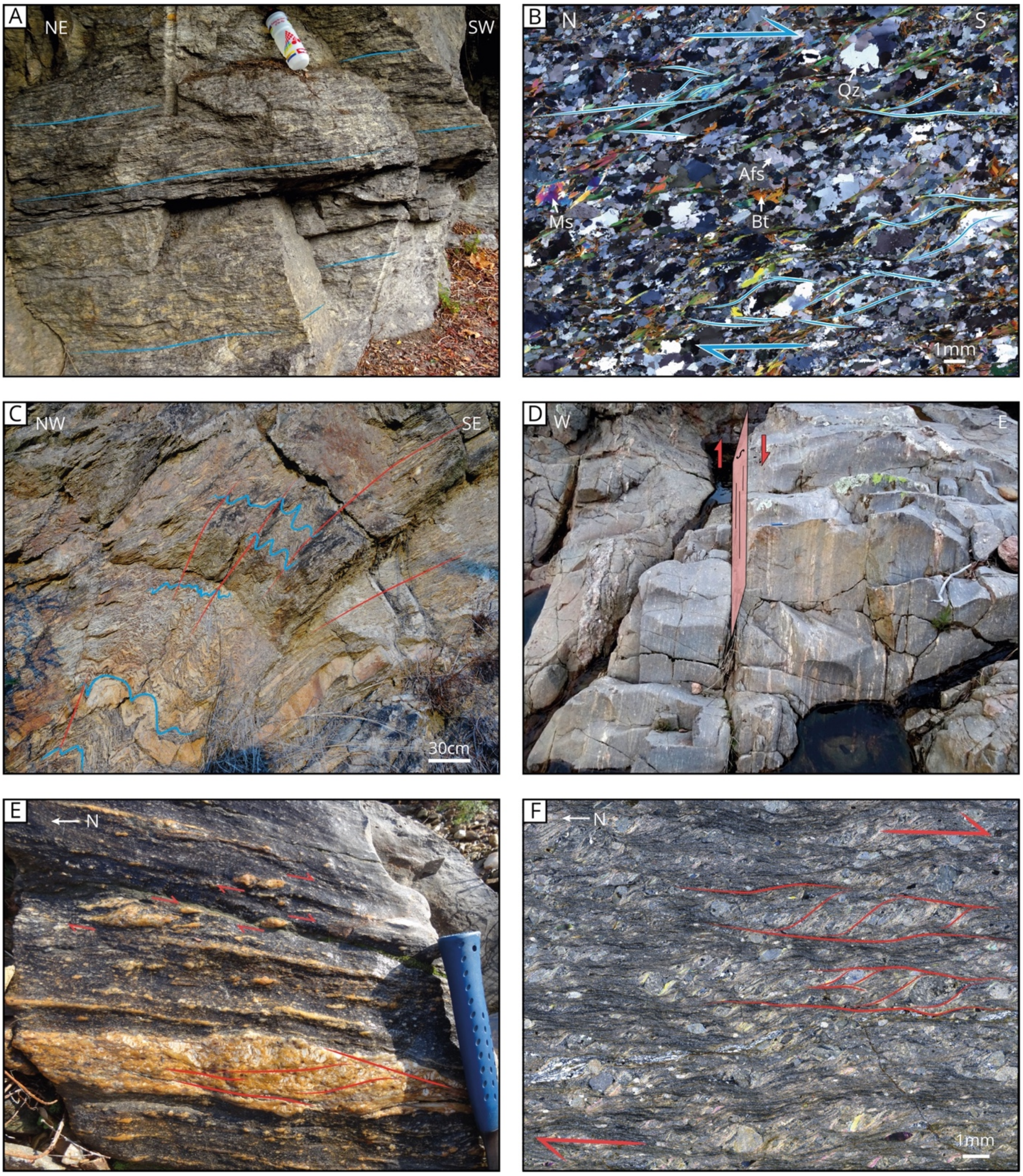

Figure 4: Geometry and kinematic of the main planar fabrics. (A) Low strain flat-lying foliation representative of S2a foliation, here in the Super Cannes hill (GPS coordinates: 43.5725/7.0678) - 3D model visible here: https://skfb.ly/oQIrH. (B) Microphotograph of a migmatitic orthogneiss in the Reyran zone displaying top to the South S/C shear structures (43.5300/6.7462). (C) S2a foliation folded and

transposed by S2b foliation, in the Croix des Gardes hill (43.5571/6.9842). (D) Representative outcrop of the La Moure SZ (and other smaller SZ) showing vertical strike-slip mylonitic S2b foliation in the migmatitic paragneiss (43.4954/6.7808). (E) Kinematic indicators giving a dextral sense of shear in mylonitic paragneiss from the La Moure SZ (43.5758/6.8274). (F) Microphotograph of an ultramylonitic paragneiss of the La Moure SZ near the contact with the Reyran basin. The texture of the highly recrystallised matrix defines widespread S/C shear bands indicating a dextral kinematic. See the intense grain size reduction until micrometric scale for this ultramylonite due to very high strain deformation at the contact with the Reyran basin (43.5412/6.7935).

Figure 5: Geometry of folds, linear fabrics and finite strain shape. (A) Microfolds with axes parallel to the stretching lineation (L2) in the Cannes migmatite (Croix des Gardes, GPS coordinates: 43.5552/6.9908) - 3D model visible here: https://skfb.ly/oQK6o. (B) Cascading open fold with a representative right angled geometry in the Cannes migmatite (Super Cannes, 43.5550/7.0615) - 3D model

visible here: https://skfb.ly/oQIqR. (C) L type tectonite in the leucocratic orthogneiss of the Reyran zone. See the absence of clear fabric in the section perpendicular to the stretching lineation (L2) (43.5528/6.8234). (D) L type tectonite in the Cannes migmatite near the Croix des Gardes hill. See the rounded shape of K-feldspars and leucosome layers encircled by biotite rims in the section perpendicular to the dominant stretching lineation (L2) (Sample JG21-19, 43.5669/6.9722) - 3D model visible here: https://skfb.ly/oQIpy. (E-F) Thin section scans of the L-type migmatitic orthogneiss sample JG21-15, with (E) XZ section parallel to the stretching lineation (L2) and (F) YZ section perpendicular to the lineation. Examples of ellipses outlined with the Ellipsfit software are shown, used for 3D finite strain ellipsoid calculation (see Methodology section). See the difference of fabrics and ellipses shape between both sections (43.5612/6.7782).

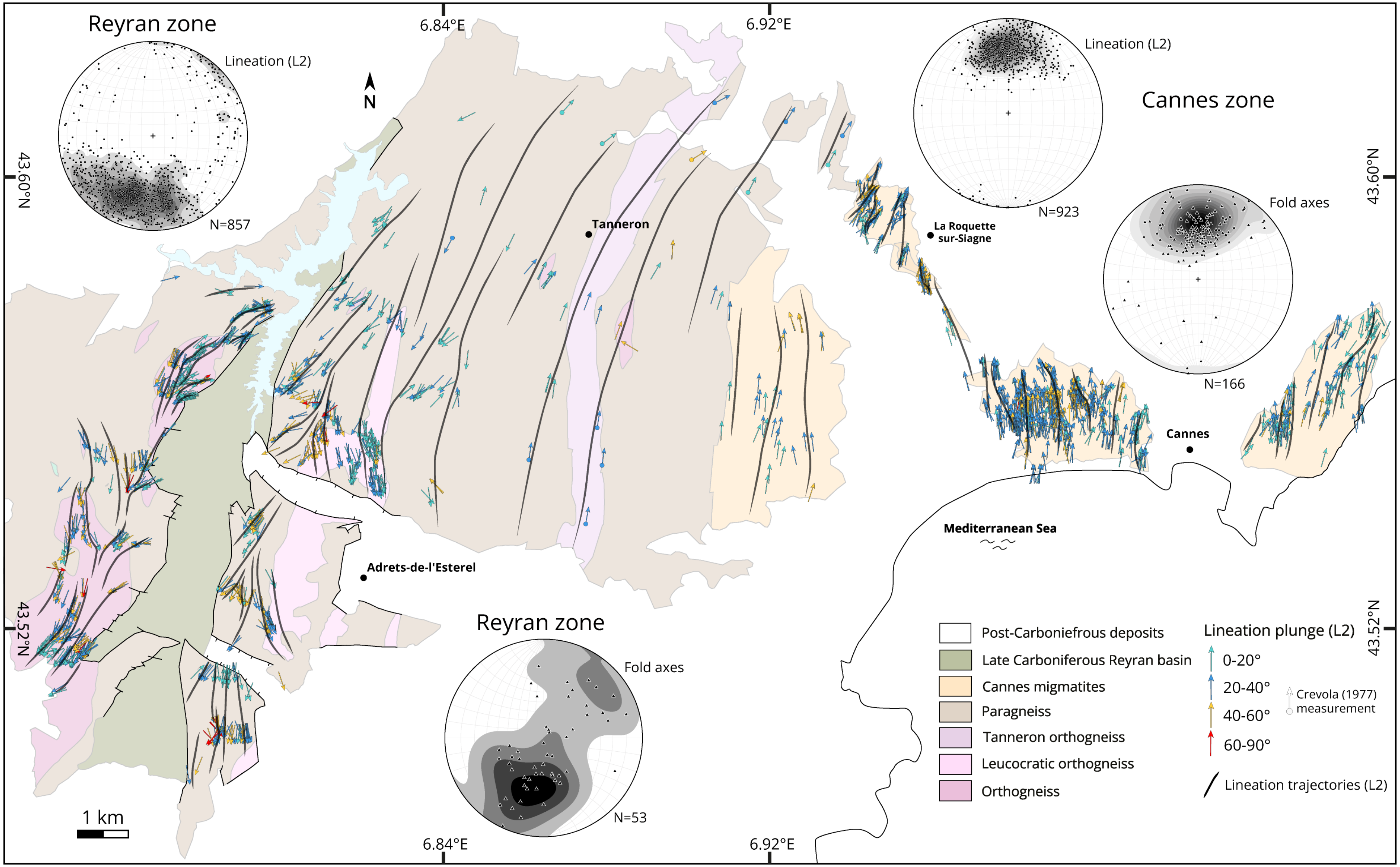
Reyran zone
Lineation (L2)
N=857
N
6.84°E
6.92°E
43.60°N
43.52°N
Tanneron
Adrets-de-l'Esterel
La Roquette sur-Siagne
Cannes
Mediterranean Sea
Cannes zone
Lineation (L2)
N=923
Fold axes
N=166
Reyran zone
Fold axes
N=53
1 km
Post-Carboniefrous deposits
Late Carboniferous Reyran basin
Cannes migmatites
Paragneiss
Tanneron orthogneiss
Leucocratic orthogneiss
Orthogneiss
Lineation plunge (L2)
0-20°
20-40°
40-60°
60-90°
Crevola (1977) measurement
Lineation trajectories (L2)

Figure 6: Structural map of lineation trajectories (L2) reflecting the N-S subhorizontal flow of the crust. The curved trails highlight convergent and divergent patterns. Lower hemisphere stereograms of lineation and fold axes for the Reyran and Cannes zone are given close to their respective area.

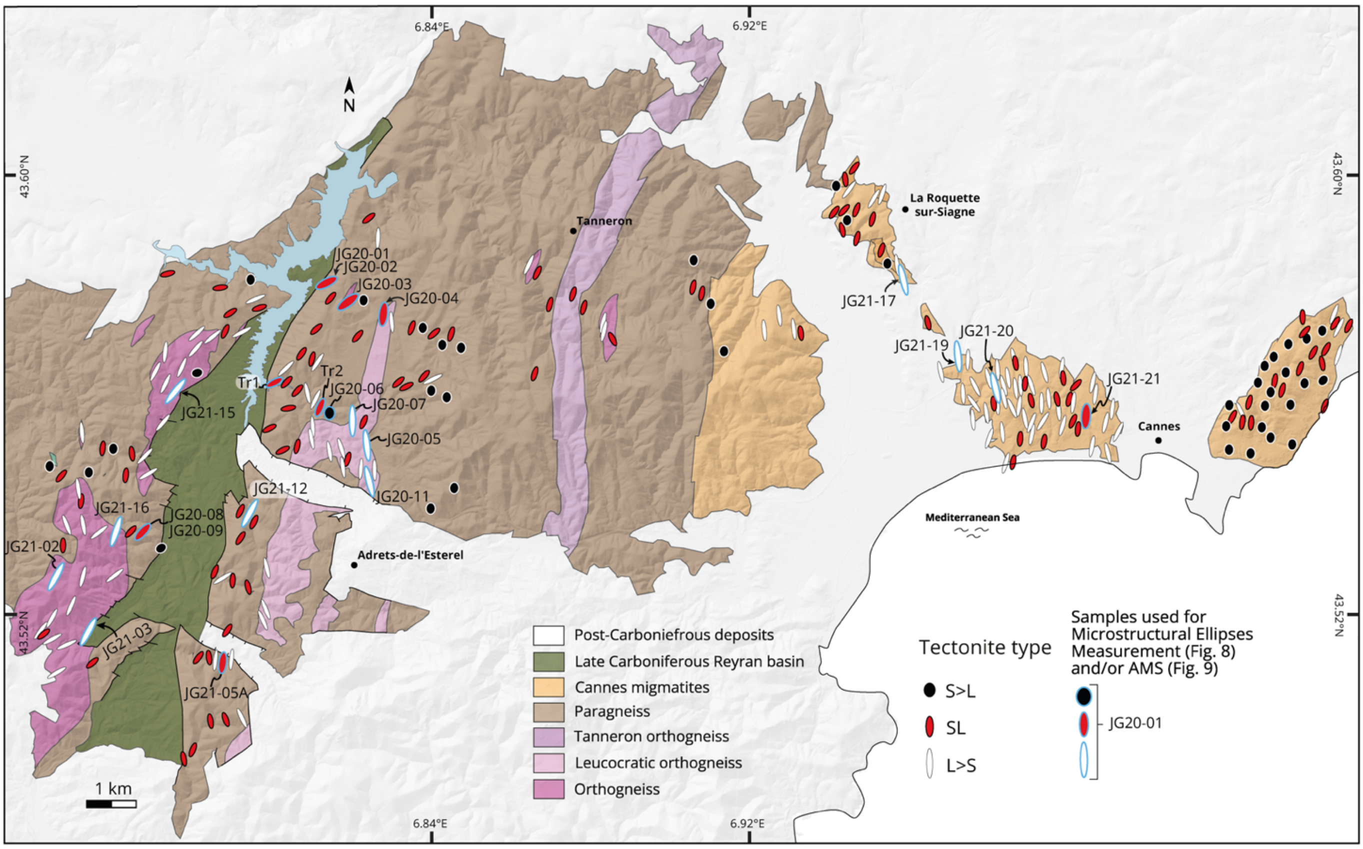

Figure 7: Tectonite-type map based on field observations of S>L, S-L, and L>S tectonites classified according to three different symbologies of ellipses varying in colour and shape. Ellipsoids corresponding to samples used for Microstructural Ellipses Measurement and/or AMS are also indicated (with a blue outline). A lithological influence is emphasised with orthogneiss showing mainly L>S tectonites whereas paragneiss are dominated by S-L tectonites. See also the contrasting tectonite type in the Cannes migmatite unit between the Croix des Gardes hill dominated by constrictional strain compared to the Super Cannes hill defining a mean flattening strain.

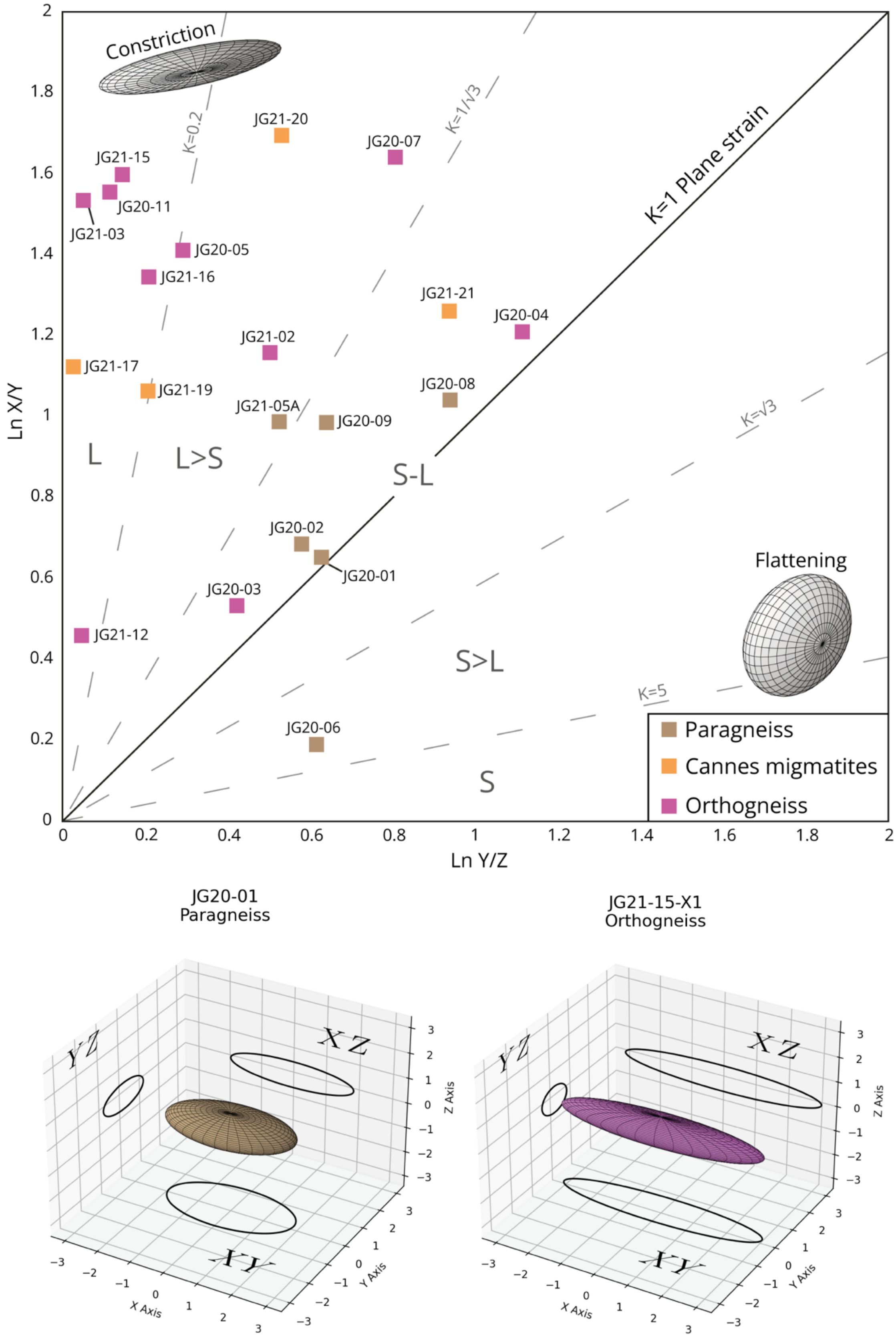
Constriction
Flattening
K=0.2
K=1/√3
K=1 Plane strain
K=√3
K=5
L
L>S
S-L
S>L
S
JG21-20
JG20-07
JG21-15
JG20-11
JG21-03
JG20-05
JG21-16
JG21-21
JG20-04
JG21-02
JG21-17
JG21-19
JG20-08
JG21-05A
JG20-09
JG20-02
JG20-01
JG20-03
JG21-12
JG20-06
Paragneiss
Cannes migmatites
Orthogneiss
Ln X/Y
Ln Y/Z
JG20-01
Paragneiss
JG21-15-X1
Orthogneiss
YZ
XZ
XY
X Axis
Y Axis
Z Axis

1500

Figure 8: Flinn diagram with plot of the 20 samples used for 3D finite strain ellipsoid calculation by microstructure measurement. Two examples of 3D finite strain ellipsoids are shown for a paragneiss and orthogneiss sample in a 3D X-Y-Z axes diagram with projection of 2D ellipses on each corresponding section. The Flinn diagram reveals a lithological control on the shape of ellipsoid with the meta-sedimentary unit mainly distributed in the S-L domain whereas meta-igneous units are mostly confined to the L and L>S domains.

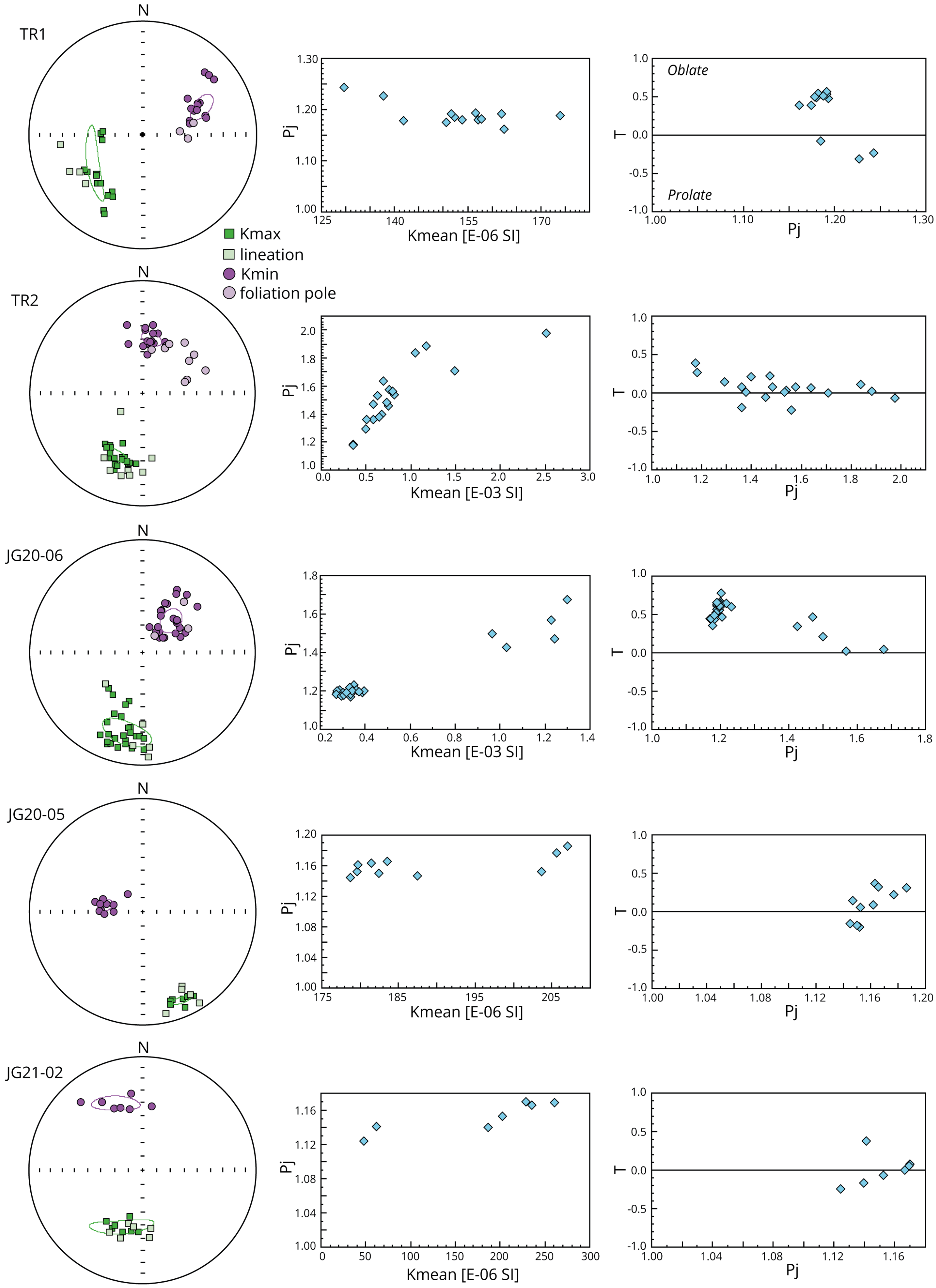
TR1
TR2
JG20-06
JG20-05
JG21-02
N
Kmax
lineation
Kmin
foliation pole
Oblate
Prolate
Pj
T
Kmean [E-06 SI]
Kmean [E-03 SI]

1508

Figure 9: AMS results with equal area, lower hemisphere projections of the principal magnetic susceptibilities axes (Kmax and Kmin), Kmean-P plot and P-T plot for each sample. Stereograms in geographical referential give foliation poles (S2) and lineations (L2) measured on each sample location compared to their AMS Kmax and Kmin values representing magnetic lineation and foliation, respectively. The confidence ellipses are computed from Jelinek's statistics (Jelinek 1978). Kmean: (Kmax+Kint+Kmin)/3; P and T parameters are used to characterise the degree of magnetic anisotropy and the AMS ellipsoid shape respectively. T ranges from -1 (prolate ellipsoid) to 1 (oblate ellipsoid) (Jelinek, 1981). Pay attention to variations in the order of magnitude of the abscissa scale.

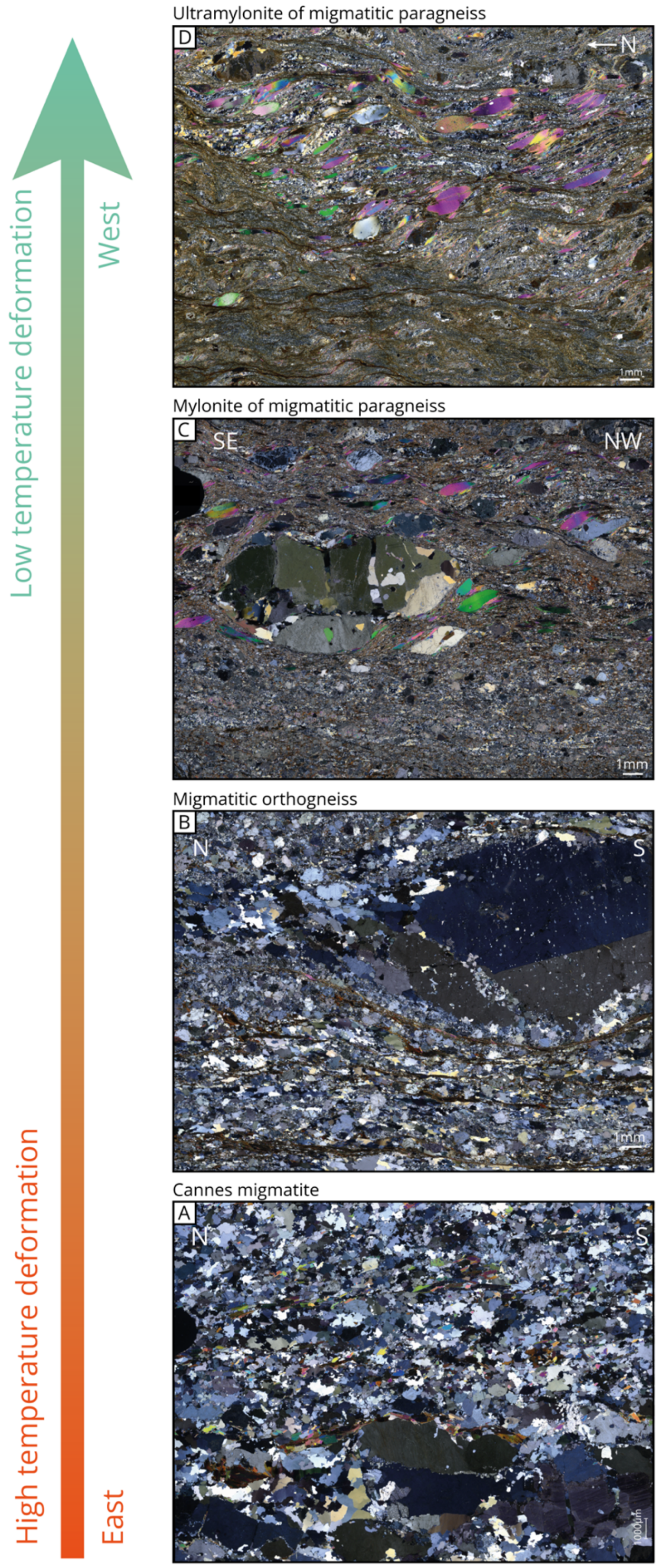
Ultramylonite of migmatitic paragneiss
D
N
1mm
Mylonite of migmatitic paragneiss
C
SE
NW
1mm
Migmatitic orthogneiss
B
N
S
1mm
Cannes migmatite
A
N
S
1000µm
Low temperature deformation
West
High temperature deformation
East

Figure 10: Microphotographs showing the evolution from high suprasolidus down to low temperature deformation through microstructure evolution. This evolution follows a broad E-W cooling gradient. Following A to D see intense grain size reduction due to increased recrystallisation and shear bands development. (A) Cannes migmatite, sample JG21-20 located in a S2a domain, showing suprasolidus deformation textures (GPS coordinates: 43.5616/6.9808). Minerals are coarse, homogenously aligned and stretched but without shear-bands, quartz is dynamically recrystallised through GBM textures, myrmekites and interstitial quartz melt infilling pore space are visible. Irregular, amoeboid quartz and feldspar boundaries are ubiquitous. (B) Migmatitic orthogneiss to the east of the La Moure SZ, sample JG20-07 located in a S2a domain, showing suprasolidus and subsolidus deformation textures (43.5119/6.7877). In fact, in the upper part the leucosome layer exhibits coarse grain size, amoeboid boundaries of GBM texture, myrmekites and interstitial quartz melt, which are characteristic of high temperature deformation. In the lower part, the grain size is smaller, discrete recrystallised shear bands are present, quartz is mostly recrystallised through SGR, indicating a colder deformation et subsolidus conditions. (C) Mylonite of migmatitic paragneiss from the outside of the La Moure SZ at the transition between S2a and S2b foliation domains, defined by middle to low temperature deformation texture (43.5579/6.8138). The main texture is a fine grain highly recrystallised matrix structured by dextral C and C’ shear bands, with quartz SGR

recrystallisation and muscovite fish. In the upper part, a preserved leucosome clast shows early high temperature deformation texture with coarse grain size, quartz GBM texture and interstitial quartz melt. (D) Ultramylonite of migmatitic paragneiss from the core of the La Moure SZ (S2b foliation) at the contact with the Reyran basin, sample JG20-01, showing low temperature deformation texture (43.5824/6.8167). The ultramylonite defines a completely recrystallised matrix of micrometric grain size (except muscovite fish) covered by a widespread anastomosed network of dextral S/C shear bands. These cold shear bands exhibit brittle-ductile deformation. Quartz is recrystallised through SGR and BLG textures. See section *“Deformation temperature”* for further detailed comments in the text.

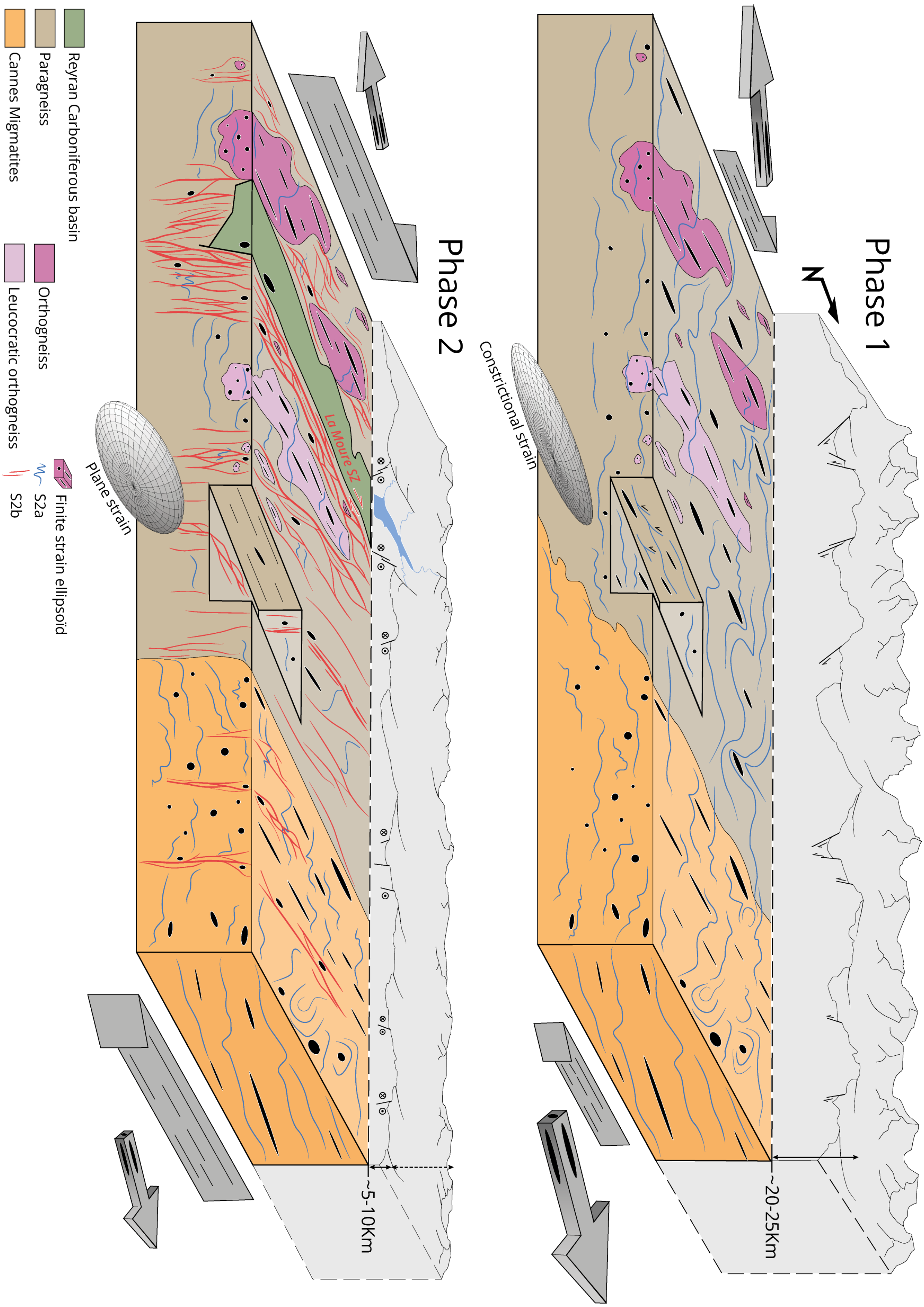
Phase 1
N
Constrictional strain
~20-25Km
Phase 2
La Moure SZ
plane strain
~5-10Km
Reyran Carboniferous basin
Paragneiss
Cannes Migmatites
Orthogneiss
Leucocratic orthogneiss
Finite strain ellipsoïd
S2a
S2b

Figure 11: Synthetic 3D diagram showing the tectonic evolution of the transtensional regime from phase 1 to phase 2. Strain patterns evolve from a first horizontal S2a foliation associated with gently dipping N-S pure shear constrictional flow, to a second vertical S2b foliation combined with simple shear plane strain flow represented by the development of an anastomosed network of local shear zones and the major La Moure SZ. During the second phase, rheologically driven strain partitioning can be seen in the preferential localisation of the plane strain flow in the paragneiss unit, enveloping orthogneiss bodies that preserved their stretched shape from the first phase. The second phase also highlights a localisation and migration of deformations from east to west, illustrated by the increasing development of the S2b foliation, which is confined to local corridors in the Cannes area and widens westwards in the Reyran area until it intensifies around the Reyran basin with the La Moure SZ.

Table 1. Finite strain ellipsoid data (Microstructural Ellipses Measurement and corresponding AMS). Max(X), Int(Y), and Min(Z) represent the three principal axes of the finite strain ellipsoids.

						Microstructural ellipses measurement				AMS	
Sample/AMS site	GPS coordinates	Lithology	Foliation (dip-dip) - S2a/b	Lineation	Field tectonite type	Max (X)	Int (Y)	Min (Z)	Ellipsoide shape	T	Ellipsoide shape
JG20-01	43.5824/6.8167	Paragneiss	297/79 - S2b	223/13	S-L	1.902	0.992	0.53	S-L		
JG20-02	43.5825/6.8167	Paragneiss	280/80 - S2b	207/06	S-L	1.914	0.966	0.541	S-L		
JG20-03	43.5783/6.8190	Orthogneiss	161/73 - S2b	240/14	S-L	1.642	0.964	0.632	S-L		
JG20-04	43.5746/6.8294	Orthogneiss	129/47 - S2a	192/33	L>S	3.244	0.968	0.318	S-L		
JG20-05	43.5523/6.8240	Orthogneiss	/	175/04	L>S	2.825	0.689	0.514	L>S	-0.2 - 0.3	S-L
JG20-06	43.5579/6.8138	Paragneiss	242/38 - S2a	176/16	S>L	1.392	1.153	0.623	S>L	0 - 0.7	S-L / S>L
JG20-07	43.5119/6.7877	Orthogneiss	93/35 - S2a	166/07	L>S	3.905	0.757	0.338	L>S		
JG20-08	43.5354/6.7671	Paragneiss	200/62 - S2b	240/35	S-L	2.738	0.967	0.378	S-L		
JG20-09	43.5355/6.7663	Paragneiss	212/66 - S2b	257/43	S-L	2.385	0.891	0.47	S-L		
JG20-11	43.5454/6.8252	Orthogneiss	168/16 - S2a	166/17	L>S	2.927	0.619	0.552	L		
JG21-02	43.5301/6.7465	Orthogneiss	/	162/43	L	2.56	0.804	0.486	L>S	-0.2 - 0.4	S-L
JG21-03	43.5169/6.7543	Orthogneiss	/	209/27	L	2.826	0.61	0.58	L		
JG21-05A	43.5119/6.7877	Paragneiss	279/51 - S2a	02/03	L>S	2.3	0.858	0.507	L>S		
JG21-12	43.5384/6.7949	Orthogneiss	268/62 - S2b	209/33	L>S	1.378	0.872	0.832	L		
JG21-15	43.5612/6.7782	Orthogneiss	/	82/05	L	3.044	0.616	0.533	L		
JG21-16	43.5355/6.7617	Orthogneiss	/	215/11	L	2.627	0.685	0.556	L		
JG21-17	43.5816/6.9591	Cannes migmatite	/	355/37	L	2.132	0.694	0.676	L		
JG21-19	43.5669/6.9722	Cannes migmatite	/	347/20	L	2.177	0.752	0.611	L		
JG21-20	43.5616/6.9808	Cannes migmatite	/	13/28	L	3.694	0.679	0.399	L>S		
JG21-21	43.5568/7.0047	Cannes migmatite	261/89 - S2b	353/14	S-L	3.165	0.898	0.352	S-L		

Table 1: Finite strain ellipsoid data (Microstructural Ellipses Measurement and corresponding AMS). Max(X), Int(Y), and Min(Z) represent the three principal axes of the finite strain ellipsoids.